AGN STORM 2: I. First results: A Change in the Weather of Mrk 817

ERIN KARA,[1] MISSAGH MEHDIPOUR,[2] GERARD A. KRISS,[2] EDWARD M. CACKETT,[3] NAHUM ARAV,[4] AARON J. BARTH,[5]
DOYEE BYUN,[4] MICHAEL S. BROTHERTON,[6] GISELLA DE ROSA,[2] JONATHAN GELBORD,[7]
JUAN V. HERNÁNDEZ SANTISTEBAN,[8] CHEN HU,[9] JELLE KAASTRA,[10,11] HERMINE LANDT,[12] YAN-RONG LI,[9]
JAKE A. MILLER,[3] JOHN MONTANO,[5] ETHAN PARTINGTON,[3] JESÚS ACEITUNO,[13,14] JIN-MING BAI,[15] DONGWEI BAO,[9,16]
MISTY C. BENTZ,[17] THOMAS G. BRINK,[18] DORON CHELOUCHE,[19,20] YONG-JIE CHEN,[9,16] ELENA DALLA BONTÀ,[21,22]
MARYAM DEHGHANIAN,[23] PU DU,[9] RICK EDELSON,[24] GARY J. FERLAND,[23] LAURA FERRARESE,[25] CARINA FIAN,[26,20]
ALEXEI V. FILIPPENKO,[18,27] TRAVIS FISCHER,[28] MICHAEL R. GOAD,[29] DIEGO H. GONZÁLEZ BUITRAGO,[30]
VAROUJAN GORJIAN,[31] CATHERINE J. GRIER,[32] WEI-JIAN GUO,[9,16] PATRICK B. HALL,[33] Y. HOMAYOUNI,[2] KEITH HORNE,[8]
DRAGANA ILIĆ,[34,35] BO-WEI JIANG,[9,16] MICHAEL D. JONER,[36] SHAI KASPI,[26] CHRISTOPHER S. KOCHANEK,[37,38]
KIRK T. KORISTA,[39] DANIEL KYNOCH,[40] SHA-SHA LI,[9,16] JUN-RONG LIU,[9,16] IAN M. MᶜHARDY,[41] JACOB N. MCLANE,[6]
JAKE A. J. MITCHELL,[12] HAGAI NETZER,[42] KIANNA A. OLSON,[6] RICHARD W. POGGE,[37,38] LUKA Č. POPOVIĆ,[43,34]
DANIEL PROGA,[44] THAISA STORCHI-BERGMANN,[45] ERIKA STRASBURGER,[18] TOMMASO TREU,[46,*]
MARIANNE VESTERGAARD,[32,47] JIAN-MIN WANG,[9,48,49] MARTIN J. WARD,[12] TIM WATERS,[50] PETER R. WILLIAMS,[46]
SEN YANG,[9,16] ZHU-HENG YAO,[9,16] THEODORA E. ZASTROCKY,[6] SHUO ZHAI,[9,16] AND YING ZU[51]

[1] MIT Kavli Institute for Astrophysics and Space Research, Massachusetts Institute of Technology, Cambridge, MA 02139, USA
[2] Space Telescope Science Institute, 3700 San Martin Drive, Baltimore, MD 21218, USA
[3] Department of Physics and Astronomy, Wayne State University, 666 W. Hancock St, Detroit, MI, 48201, USA
[4] Department of Physics, Virginia Tech, Blacksburg, VA 24061, USA
[5] Department of Physics and Astronomy, 4129 Frederick Reines Hall, University of California, Irvine, CA, 92697-4575, USA
[6] Department of Physics and Astronomy, University of Wyoming, Laramie, WY 82071, USA
[7] Spectral Sciences Inc., 4 Fourth Ave., Burlington, MA 01803, USA
[8] SUPA School of Physics and Astronomy, North Haugh, St. Andrews, KY16 9SS, Scotland, UK
[9] Key Laboratory for Particle Astrophysics, Institute of High Energy Physics, Chinese Academy of Sciences, 19B Yuquan Road,
Beijing 100049, People's Republic of China
[10] SRON Netherlands Institute for Space Research, Sorbonnelaan 2, 3584 CA Utrecht, The Netherlands
[11] Leiden Observatory, Leiden University, PO Box 9513, 2300 RA Leiden, The Netherlands
[12] Centre for Extragalactic Astronomy, Department of Physics, Durham University, South Road, Durham DH1 3LE, UK
[13] Centro Astronomico Hispano Alemán, Sierra de los filabres sn, E-04550 Gérgal, Almería, Spain
[14] Instituto de Astrofísica de Andalucía (CSIC), Glorieta de la astronomía sn, E-18008 Granada, Spain
[15] Yunnan Observatories, The Chinese Academy of Sciences, Kunming 650011, People's Republic of China
[16] School of Astronomy and Space Science, University of Chinese Academy of Sciences, 19A Yuquan Road, Beijing 100049, China
[17] Department of Physics and Astronomy, Georgia State University, 25 Park Place, Suite 605, Atlanta, GA 30303, USA
[18] Department of Astronomy, University of California, Berkeley, CA 94720-3411, USA
[19] Department of Physics, Faculty of Natural Sciences, University of Haifa, Haifa 3498838, Israel
[20] Haifa Research Center for Theoretical Physics and Astrophysics, University of Haifa, Haifa 3498838, Israel
[21] Dipartimento di Fisica e Astronomia "G. Galilei," Universitá di Padova, Vicolo dell'Osservatorio 3, I-35122 Padova, Italy
[22] INAF-Osservatorio Astronomico di Padova, Vicolo dell'Osservatorio 5 I-35122, Padova, Italy
[23] Department of Physics and Astronomy, The University of Kentucky, Lexington, KY 40506, USA
[24] Eureka Scientific Inc., 2452 Delmer St. Suite 100, Oakland, CA 94602, USA
[25] NRC Herzberg Astronomy and Astrophysics Research Centre, 5071 West Saanich Road, Victoria, BC, V9E 2E7, Canada
[26] School of Physics and Astronomy and Wise observatory, Tel Aviv University, Tel Aviv 6997801, Israel
[27] Miller Institute for Basic Research in Science, University of California, Berkeley, CA 94720, USA
[28] AURA for ESA, Space Telescope Science Institute, Baltimore, MD, USA, 3700 San Martin Drive, Baltimore, MD 21218, USA
[29] School of Physics and Astronomy, University of Leicester, University Road, Leicester, LE1 7RH, UK
[30] Instituto de Astronomía, Universidad Nacional Autónoma de México, Km 103 Carretera Tijuana-Ensenada, 22860 Ensenada B.C.,
México
[31] Jet Propulsion Laboratory, M/S 169-327, 4800 Oak Grove Drive, Pasadena, CA 91109, USA
[32] Steward Observatory, University of Arizona, 933 North Cherry Avenue, Tucson, AZ 85721, USA
[33] Department of Physics and Astronomy, York University, Toronto, ON M3J 1P3, Canada
[34] Department of Astronomy, Faculty of Mathematics, University of Belgrade, Studentski trg 16,11000 Belgrade, Serbia
[35] Humboldt Research Fellow, Hamburger Sternwarte, Universität Hamburg, Gojenbergsweg 112, 21029 Hamburg, Germany
[36] Department of Physics and Astronomy, N283 ESC, Brigham Young University, Provo, UT 84602, USA

[37] *Department of Astronomy, The Ohio State University, 140 W. 18th Ave., Columbus, OH 43210, USA*

[38] *Center for Cosmology and AstroParticle Physics, The Ohio State University, 191 West Woodruff Ave., Columbus, OH 43210, USA*

[39] *Department of Physics, Western Michigan University, 1120 Everett Tower, Kalamazoo, MI 49008-5252, USA*

[40] *Astronomical Institute of the Czech Academy of Sciences, Boční II 1401/1a, CZ-14100 Prague, Czechia*

[41] *School of Physics and Astronomy, University of Southampton, Highfield, Southampton SO17 1BJ, UK*

[42] *School of Physics and Astronomy, Tel Aviv University, Tel Aviv 69978, Israel*

[43] *Astronomical Observatory, Volgina 7, 11060 Belgrade, Serbia*

[44] *Department of Physics & Astronomy, University of Nevada, Las Vegas 4505 S. Maryland Pkwy, Las Vegas, NV, 89154-4002, USA*

[45] *Departamento de Astronomia - IF, Universidade Federal do Rio Grande do Sul, CP 150501, 91501-970 Porto Alegre, RS, Brazil*

[46] *Department of Physics and Astronomy, University of California, Los Angeles, CA 90095, USA*

[47] *DARK, The Niels Bohr Institute, University of Copenhagen, Jagtvej 128, DK-2200 Copenhagen, Denmark*

[48] *School of Astronomy and Space Sciences, University of Chinese Academy of Sciences, 19A Yuquan Road, Beijing 100049, People's Republic of China*

[49] *National Astronomical Observatories of China, 20A Datun Road, Beijing 100020, People's Republic of China*

[50] *Department of Physics & Astronomy, University of Nevada, Las Vegas 4505 S. Maryland Pkwy, Las Vegas, NV, 89154-4002, USA*

[51] *Department of Astronomy, School of Physics and Astronomy, Shanghai Jiao Tong University, Shanghai 200240, China*

ABSTRACT

We present the first results from the ongoing, intensive, multi-wavelength monitoring program of the luminous Seyfert 1 galaxy Mrk 817. While this AGN was, in part, selected for its historically unobscured nature, we discovered that the X-ray spectrum is highly absorbed, and there are new blueshifted, broad and narrow UV absorption lines, which suggest that a dust-free, ionized obscurer located at the inner broad line region partially covers the central source. Despite the obscuration, we measure UV and optical continuum reverberation lags consistent with a centrally illuminated Shakura-Sunyaev thin accretion disk, and measure reverberation lags associated with the optical broad line region, as expected. However, in the first 55 days of the campaign, when the obscuration was becoming most extreme, we observe a de-coupling of the UV continuum and the UV broad emission line variability. The correlation recovers in the next 42 days of the campaign, as Mrk 817 enters a less obscured state. The short C IV and Lyα lags suggest that the accretion disk extends beyond the UV broad line region.

Keywords: accretion, accretion disks — black hole physics — line: formation – X-rays, UV, optical: individual (Mrk 817)

1. INTRODUCTION

For nearly two decades, quasars have been regarded as critical elements in our understanding of galaxy evolution. Without energetic quasar outflows in the forms of radiation, winds, or radio jet plasma, galaxy evolution models overpredict the luminosities of galaxies at the bright end of the luminosity function (Croton et al. 2006; Fabian et al. 2012). Quasar outflows may provide feedback that can heat or remove the interstellar medium of the host galaxy. This can shut down star formation and terminate the gas flow to the black hole, thus freezing the total stellar luminosity and black hole mass and leaving a quiescent black hole at the center of a dead (non-star-forming) galaxy (e.g. Hopkins et al. 2008). The otherwise baffling correlations between the mass of the central supermassive black hole and gross observable properties of the host galaxy (e.g., bulge velocity dispersion or luminosity) are naturally explained by this feedback (Ferrarese & Merritt 2000; Gebhardt et al. 2000; Yu & Tremaine 2002). However, direct observational evidence of quasar feedback has remained elusive.

Among the processes that are poorly understood are the gas flows and their origin near the central black hole. There is ample evidence of large-scale, high-velocity outflows from blueshifted X-ray absorption lines (e.g., Pounds et al. 2003; Tombesi et al. 2010; Parker et al. 2017) and UV spectra (e.g., Kriss et al. 2018) – however, the information gleaned from this is only along the line of sight, only in the resonance lines, and is difficult to convert into mass flows because of the unknown covering factor and unknown physical distance of the absorber to the black hole. With the rare exceptions of recent interferometric observations of AGN including 3C273 (GRAVITY Collaboration et al. 2018) and

NGC 3783 (GRAVITY Collaboration et al. 2021), the centi-parsec scales of AGN in the UV/optical are too small to be directly resolvable. Resolving micro-parsec scales of the X-ray emitting region is even less attainable, except for the notable exception of the sub-mm image of the low-luminosity AGN in M87 (Event Horizon Telescope Collaboration et al. 2019). Consequently the most powerful tool available to probe active nuclei is reverberation mapping (RM), which substitutes time resolution for spatial resolution (Blandford & McKee 1982).

The reverberation mapping technique was pioneered in the optical, where the location and motion of gas flows that constitute the "broad-line region" (BLR) are constrained by observing the time-delayed response of broad emission lines to the variable continuum flux from the black hole accretion disk (e.g. Peterson 1993; Bentz et al. 2009). In recent years, higher cadence observing campaigns at shorter wavelengths has allowed for reverberation mapping of the continuum-emitting accretion disk in the UV/optical (e.g. Edelson et al. 2015; Cackett et al. 2018), and even within the inner tens of gravitational radii with X-ray reverberation (e.g. Uttley et al. 2014).

The UV wavelength regime is particularly important for understanding the inner centi-parsec gas flows in AGN using RM because of the presence of two of the strongest and most important diagnostic emission lines, C IV $\lambda\lambda$1548, 1551, and Lyα λ1215. Moreover, the UV continuum arises primarily in the inner accretion disk and is a better proxy than the optical continuum for the unobservable ionizing continuum that drives the line variations.

Several pioneering AGN UV spectral monitoring programs were undertaken with the International Ultraviolet Explorer (IUE) and the Hubble Space Telescope (HST) in the late 1980s and 1990s. These early campaigns led to an understanding of the practicalities of RM that informed more intensive campaigns, intended to determine not only sizes of the line-emitting regions, but also their kinematics (e.g., Horne et al. 2004). While ground-based optical campaigns designed for velocity-dependent RM (2D RM) have achieved great success, there has only been one 2D RM program in the UV. This study of NGC 5548 is known as the AGN Space Telescope and Optical Reverberation Mapping program (AGN STORM; e.g. De Rosa et al. 2015; Kriss et al. 2019b). Here we present the first results from a second such program, this time on Mrk 817. We refer to the new campaign as AGN STORM 2, and henceforth refer to the NGC 5548 campaign as AGN STORM 1.

The AGN STORM 1 program was a multiwavelength spectroscopic and photometric monitoring campaign that was undertaken in the first half of 2014 (HST Cycle 21), anchored by nearly daily observations of NGC 5548 over six months with the HST Cosmic Origins Spectrograph (COS). The HST observations were supplemented by high-cadence (approximately twice daily) X-ray and near-UV observations with Swift (Edelson et al. 2015), as well as intensive ground-based optical photometric (Fausnaugh et al. 2016a) and spectroscopic (Pei et al. 2017) monitoring, plus four observations with Chandra (Mathur et al. 2017).

AGN STORM 1 yielded a number of surprising results. The single most important lesson from this campaign is that intensive multi-wavelength monitoring enables us to decipher the relationships between different spectral properties including the presence (or lack) of reverberation, and the role of obscuration in the reprocessing of radiation. Among the interesting and unexpected results from AGN STORM 1 are the following:

1. Longer-wavelength continuum variations follow shorter-wavelength continuum variations from the UV through the NIR in a pattern largely consistent with the temperature gradient expected from a standard Shakura–Sunyaev thin accretion disk (Shakura & Sunyaev 1973), but suggesting a disk that is three times larger (Edelson et al. 2015; Fausnaugh et al. 2016a; Starkey et al. 2017). However, the X-ray variations and those at longer wavelengths are not simply related (e.g., Gardner & Done 2017; Edelson et al. 2019).

2. The emission-line lags were much smaller than expected from the well-established relationship between the AGN luminosity and the time-delayed response of the broad emission lines. Given the luminosity of NGC 5548 and its past behavior, the expected Hβ lag was ~ 20 days, but the observed delay was only ~ 6 days (Pei et al. 2017).

3. The time lag between the UV and optical continuum variations is the same as the time lag between the UV continuum variations and the most rapidly responding emission lines (He II λ1640 and He II λ4686, ~ 2 days; Fausnaugh et al. 2016b).

4. During part of the AGN STORM 1 program, all of the emission lines and the high-ionization absorption lines apparently decoupled from the continuum variations (the so-called "BLR holiday" of Goad et al. 2016).

5. The "velocity-delay maps," i.e., the projection of the BLR into the two observables of time delay and line-of-sight velocity, suggest the presence of
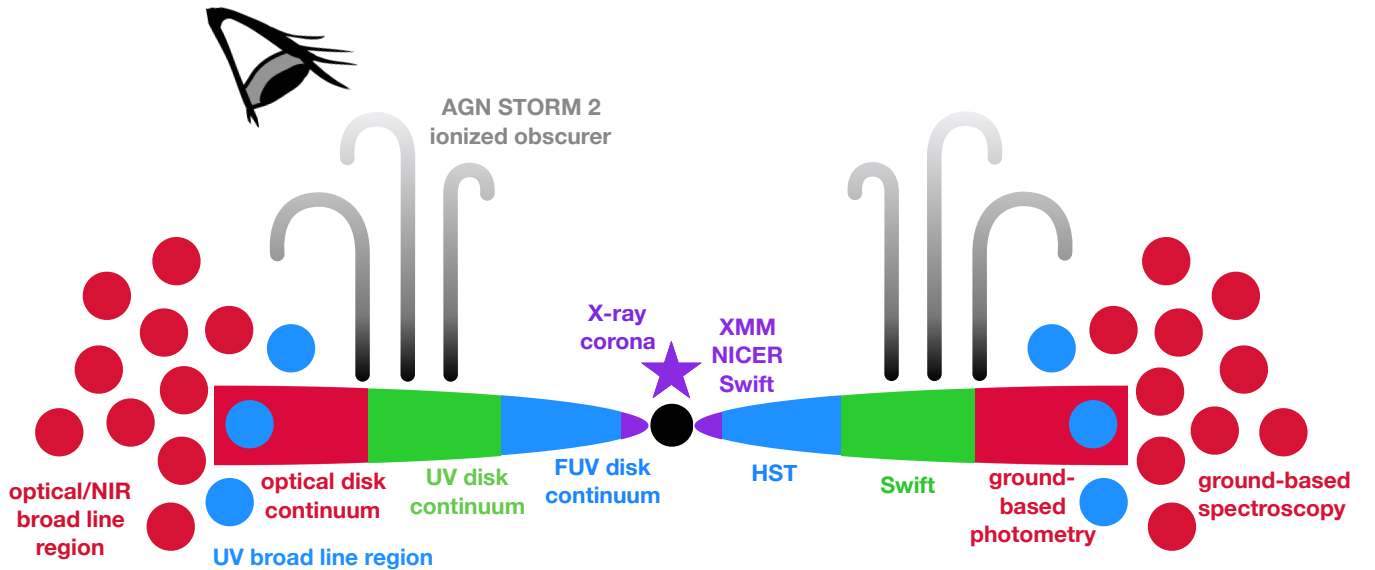
Figure 1. Schematic overview of the AGN STORM 2 campaign, highlighting the telescopes involved thus far, and what regions they probe. The color schemes correspond to different telescopes/wavelength regimes, and will be used throughout this paper and future papers. The most unexpected result is the presence of a new dust-free ionized wind, as evidenced by the presence of new narrow and broad UV absorption lines (Fig 2), and a significant depression of soft X-rays relative to earlier observations (Fig. 3). Spectral decomposition (Section 3.1.1, Section 3.1.2) and photoionization modelling (Section 3.3) place the new absorber at the inner broad line region. Despite this unexpected wind, the optical/UV continuum reverberation lags appear to behave as expected for reprocessing in a standard thin disk (Section 3.4.1 and Fig. 13). The broad line region reverberation is more complex, as the Hβ lags behave as expected, but the UV broad emission lines are uncorrelated with the continuum for the first ~ 60 days, likely due to interference from the obscurer (Section 3.4.2 and Fig. 14).

an inclined disk, but the response of the far side of the disk is weaker than expected (Horne et al. 2021). Direct modeling of the spectra yields similar results (Williams et al. 2020).

The emission-line and absorption-line behaviors can be explained by an "obscurer" (cf., Kaastra et al. 2014a) that is located in the inner BLR and associated with the broad absorption seen in the short wavelength wings of the broad resonance emission lines. The properties of the obscurer are consistent with a disk wind that is launched from the inner BLR, and whose absorption alters the SED seen by more distant emission components. Instabilities in the density of the base of the wind cause variations in the line of sight covering factor (Dehghanian et al. 2019, 2020, 2021). The existence of an obscurer in NGC 5548 underscored the importance of contemporaneous X-ray observations. This enables us to determine the SED that is incident upon the obscurer, and the SED that is filtered by the obscurer and reaches the BLR.

In this paper, we present the first results from a second intensive multiwavelength campaign intended to study gas flows, as manifested in both emission and absorption lines, in the vicinity of a supermassive black hole. The target of this new campaign is Mrk 817 (PG 1434+590).

Mrk 817 was selected for this campaign based on a number of considerations, both scientific and practical:

1. There is no historical evidence for the type of broad UV absorption lines that complicated the interpretation of the NGC 5548 data. We believed that the sightline to the BLR and accretion disk would be clear and unobscured.

2. Mrk 817 affords an opportunity to explore a different part of AGN parameter space; its mass ($M_{\rm BH} \approx 3.85 \times 10^7\,M_\odot$) is similar to that of NGC 5548 but it is more luminous and so has a higher Eddington ratio ($L/L_{\rm Edd} \sim 0.2$ for Mrk 817, and $L/L_{\rm Edd} \sim 0.03$ for NGC 5548).

3. The Galactic foreground extinction is low, $E(B-V) \approx 0.02\,{\rm mag}$, and Mrk 817 is close enough to the north ecliptic pole that it can be observed throughout the year by HST and other satellites and moderate-to-high latitude ground-based observatories.

In this paper, we discuss some early results and findings from the first third of the campaign. These early results do not incorporate planned improvements to the COS and STIS calibrations that are also part of our ongoing program. Final results upon completion of the program may differ slightly from those presented here.

The biggest surprise in our observations was that there are now both broad and narrow absorption features in the UV spectra, and the X-rays show that the ionizing continuum is heavily obscured (see schematic in Fig 1). This appears to have induced a "broad line holiday" as the broad UV emission lines in the early part of the campaign do not respond coherently to UV continuum variations. Remarkably, however, the broad Hβ emission line does appear to lag behind the continuum with the time delay expected from the radius-luminosity relation (Bentz et al. 2013).

The paper is organized as follows: In Section 2, we describe the data from the space and ground-based telescopes involved in the campaign. In Section 3.1, we present the detailed spectral modelling of the long HST STIS and COS observation (Visit 3N) and a long XMM-Newton stare, both taken on 2020-12-18. We focus on characterizing the new ionized obscurer, and in Section 3.2, we put the results into the context of the overall AGN STORM 2 campaign thus far (97 days, from 2020-11-11 to 2021-03-01; HJD 2459177-2459274). Next, in Section 3.3, we present photoionization models for the narrow and broad UV absorption lines, given the ionizing broadband SED from the 2020-12-18 observations. Finally in 3.4, we present preliminary UV/optical continuum and broad line region reverberation mapping.

2. OBSERVATIONS AND DATA REDUCTION

2.1. *HST COS and STIS*

The HST observing program (GO Proposal ID 16196) began a 1-year campaign on 2020-11-24. Using the Cosmic Origins Spectrograph (COS; Green et al. 2012), we obtain medium resolution UV spectra covering 1070–1750 Å in one-orbit visits scheduled on an approximately two-day cadence. Each visit consists of four 60 s exposures with grating G130M at the 1222Å central wavelength setting and all four focal-plane (FP-POS) positions, exposures of 175 s and 180 s using G160M at the 1533Å central wavelength setting at two FP-POS locations, and two 195 s exposures with G160M at the 1577Å central wavelength setting also at two FP-POS locations. The multiple grating settings and FP-POS locations permit us to sample the detector at four locations for each wavelength to correct for flat-field anomalies, grid-wire shadows, and gain sag in the detector (Dashtamirova & Fischer 2020). For our analysis we use the calibrated spectra from the Mikulski Archive for Space Telescopes (MAST) as processed by version 3.3.10 of the COS calibration pipeline. The pipeline assembles the individual exposures into three combined spectra for each grating setting. We then combine these three spectra using the IRAF task `splice` to form the merged 1070–1750 Å final product.

Our observing program also includes monthly observations of the flux standard WD0308−565 using the same grating settings, which will permit us to track the time-dependent sensitivity of COS more precisely. We are not yet incorporating these potential corrections into the data presented here, which have calibration accuracies of ∼5% in absolute flux, ∼2% in day-to-day reproducibility, and a wavelength accuracy of ∼ 5 km s^{-1} (Dashtamirova & Fischer 2020).

Our first spectrum revealed unexpected, strong, broad, blueshifted absorption lines similar to the obscuring outflows seen in other Seyfert galaxies such as Mrk 335 (Longinotti et al. 2013), NGC 5548 (Kaastra et al. 2014b), NGC 985 (Ebrero et al. 2016) and NGC 3783 (Mehdipour et al. 2017). To obtain a full range of spectral diagnostics for understanding the new obscuring outflow in Mrk 817, we arranged our observing program to include additional COS exposures covering shorter wavelengths down to 940 Å, together with the scheduled Space Telescope Imaging Spectrograph (STIS; Woodgate et al. 1998) spectra covering longer wavelengths up to 1 μm.

The additional COS spectra were obtained during Visit 3N on 2020-12-18, simultaneously with the XMM-Newton observation. They comprised four 522 s exposures at all four FP-POS settings with grating G130M at the 1096 central wavelength setting. When combined with the standard G130M and G160M exposures, the merged spectrum covers 940–1750 Å, as shown in Fig.2. The STIS exposures all used the 52x0.5 arcsec slit. With grating G230L and the NUV-MAMA, a 320 s exposure covered 1600–3150 Å. For the longer wavelengths we used the STIS CCD and a series of of CR-SPLIT exposures at three points along the slit to eliminate hot and cold pixels from the final spectra. Using grating G430L three 30 s exposures covered 2950–5700 Å, and three 30 s exposures with grating G750L covered 5300–10,200 Å.

With a continuum flux at 1398 Å of 7.7×10^{-14} erg cm^{-2} s^{-1} Å^{-1}, Mrk 817 has so far in our campaign been substantially brighter than the mean historical flux of 4.3×10^{-14} erg cm^{-2} s^{-1} Å^{-1} at 1397 Å (Dunn et al. 2006). Our spectrum shows a rich range of broad absorption lines– S VI $\lambda\lambda$933,944, C III λ977, N III $\lambda\lambda$989,991, O VI $\lambda\lambda$1031,1037, P V $\lambda\lambda$1117,1128, C III* λ1176, N V $\lambda\lambda$1238,1242, Si IV $\lambda\lambda$1393,1402, C IV $\lambda\lambda$1548,1550, and Lyman lines from α through δ.

In addition to these new, broad absorption features, the other intrinsic absorption lines in Mrk 817 show continuing variability. The first observation with COS in 2009 by Winter et al. (2011) showed changes in sev-
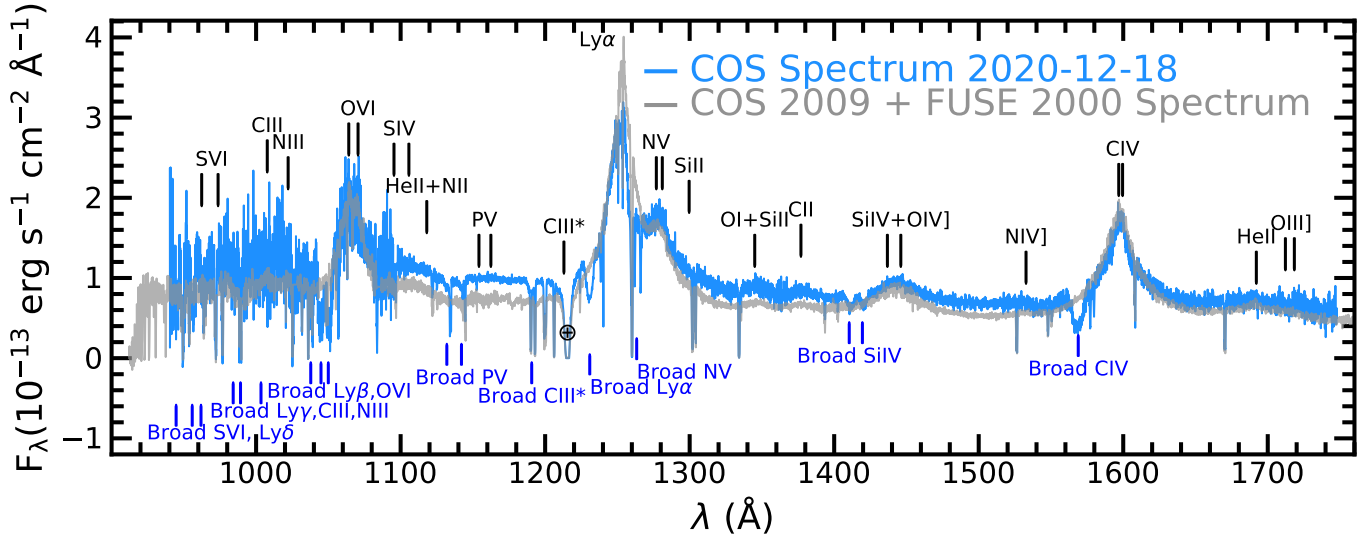
Figure 2. The COS spectrum of Mrk 817 from 2020-12-18 (blue), compared to archival spectra (gray) from COS (in 2009; Winter et al. 2011) and FUSE (in 2000; Kriss 2001). The COS data are binned by 8 pixels (∼1 resolution element). Positions of typical AGN emission features are labeled above the spectrum, and new broad absorption features detected in 2020 are labeled in blue. Geocoronal emission is indicated with an Earth symbol in the center of the Milky Way Lyα absorption trough, and has been removed.
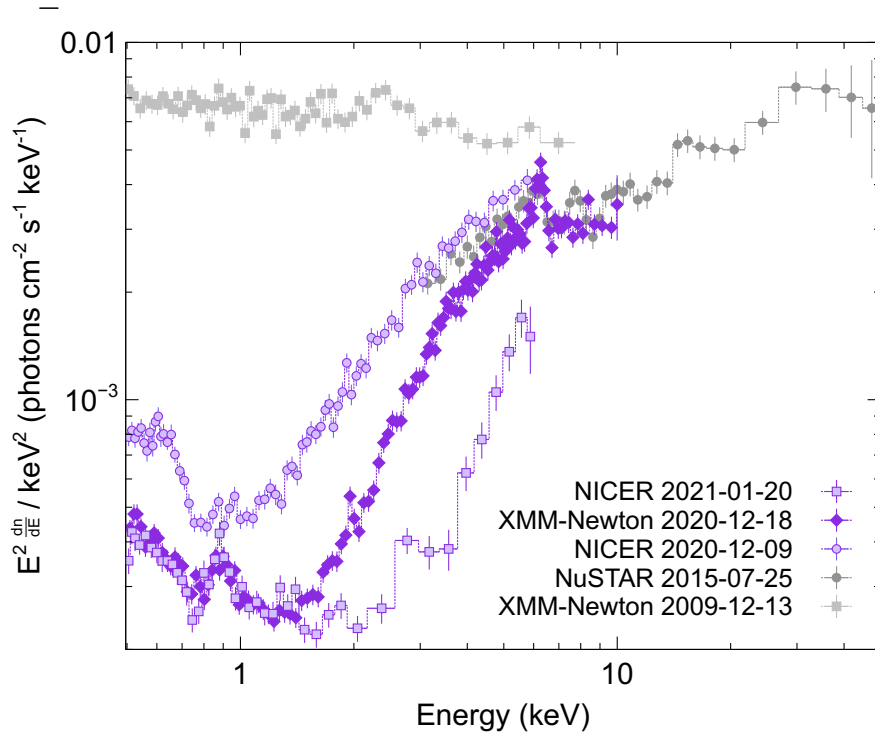
Figure 3. X-ray counts multiplied by an E^2 powerlaw, illustrating the change in spectral shape between earlier observations from XMM-Newton in 2009 and NuSTAR in 2015 (gray), and the new observations (XMM-Newton in purple diamonds and NICER in lighter purple circles).

eral lines compared to prior HST observations. In our observations, the absorption lines described by Winter et al. (2011) have weakened, and a new strong system of features at $v_{\mathrm{out}} = -3720$ km s^{-1} has appeared. We measured velocities relative to the preferred systemic redshift in the NASA Extragalactic Database[1] (NED) of z=0.031455 from Strauss & Huchra (1988). This new system shows absorption exclusively by high-ionization ions: S VI $\lambda\lambda$933,944, O VI $\lambda\lambda$1031,1037, N V $\lambda\lambda$1238,1242, C IV $\lambda\lambda$1548,1550, Lyα, and Lyβ.

2.2. *XMM-Newton*

Upon discovery of the unexpected features in the COS spectra and reduced soft X-ray flux indicated by Swift and NICER, we requested a 135 ks XMM-Newton Director's Discretionary Time (DDT) observation (PI: N. Schartel). The observation (OBSID: 0872390901) took place on 2020-12-18. We reduced the data using the *XMM-Newton* Science Analysis System (SAS v. 19.0.0) and the newest calibration files. We started with the observation data files and followed standard procedures. The observations were taken in Large Window Mode. The source extraction regions are circular regions of radius 35 arcsec centered on source position. The background regions are also circular regions of radius 35 arcsec, avoiding the detector edges where the instrumental copper line is most prominent. The observations were relatively clean of soft proton background flares, save for a few kiloseconds removed from the end of the observation, for a final exposure of 115 ks. The response matrices were produced using rmfgen and arfgen in SAS. The PN spectra were binned to a minimum of 25 counts per bin to enable the use of χ^2 statistic. The 2020-12-18 PN observation is shown in purple in Fig. 3, compared to the only archival XMM-Newton observation, a 15 ks observation taken in 2009 when the source was significantly brighter in X-rays (light grey; Winter et al. 2011).

The XMM-Newton/RGS data were reduced using the standard pipeline tool, RGSPROC, which produces the source, background spectral files, and instrument response files. We binned the RGS 1 and 2 spectra with 'optimal binning' Kaastra & Bleeker (2016), and fit the combined spectrum with the Cash statistic. Upon inspection of the RGS spectra, we discovered that the spectrum was dispersed such that a nearby star falls on the RGS detector and contaminates the background direction. This causes artificial 'absorption' features in the background-subtracted spectrum, and also means that the RGS continuum is somewhat contaminated. We account for this by allowing the RGS to have a

different continuum level from the PN spectrum. Future XMM-Newton observations of Mrk 817 during the AGN STORM 2 campaign will have a different position angle to avoid this star.

2.3. *NuSTAR*

The 2020-12-18 XMM-Newton DDT observation was taken concurrently with NuSTAR observations (PI: J. Miller; NuSTAR GO Cycle 6). These NuSTAR results were recently published in Miller et al. (2021), and corroborate spectral modelling shown here to the XMM-Newton observations. Here, we use the publicly available NuSTAR observations that took place on 2015-07-25 for 21 ks (obsid: 60160590002). The NuSTAR Level 1 data products were processed with the NuSTAR Data Analysis Software (NUSTARDAS v2.0), and the cleaned Level 2 event files were produced and calibrated with the standard filtering criteria using the NUPIPELINE task and CALDB version 20200813. The source and background regions were circular regions of radius 60 arcsec. The spectra were binned in order to oversample the instrumental resolution by a factor of three and to have a signal-to-noise of greater than 3σ in each bin.

The resulting NuSTAR spectrum is shown in Fig. 3. In Section 3.1.2, we fit the XMM-Newton spectra together with the archival NuSTAR spectrum. While not simultaneous with our current campaign, it does not appear that the hard X-ray flux has changed significantly, consistent with the idea that most of the variability is due to line-of-sight obscuration. In particular, note that the 2015 NuSTAR and December 2020 XMM-Newton observations overlap in the 6–10 keV range.

2.4. *NICER*

NICER started monitoring Mrk 817 on 2020-11-28 (HJD 2459181) with an approximate cadence of every other day as part of a TOO request (PI: E. Cackett, Target ID: 320186). The data were processed using NICER data-analysis software version 2019-05-21_V006 and CALDB version xti20200722 with the energy scale (gain) version "optmv10". Short duration (typically < 100 s) background flares were filtered out by excluding time intervals with a 13-15 keV count rate greater than 0.12 c s^{-1}, and spectra for each observation were constructed with the background estimator known as 3C50 (Remillard et. al, submitted). Events were screened for overall high background rates using the level 3 filtering described in Remillard et. al, rejecting 1 observation. 14 observations with a mean overshoot rate higher than 0.28, corresponding to a high particle background which could not be modelled with confidence and were not identified by the 3C50 method, were also rejected.

---

[1] ned.ipac.caltech.edu

The remaining 33 observations were divided into five time intervals, and the background-subtracted spectra within each interval were combined using addspec. Each combined spectrum was grouped using the 'optimal binning' scheme (Kaastra & Bleeker 2016), with a minimum of 25 counts per bin. Two NICER spectra from towards the beginning and end of the time period we consider here are shown in Fig. 3, demonstrating the evolution of the soft X-ray emission.

2.5. *Neil Gehrels Swift Observatory*

Swift (Gehrels et al. 2004) began monitoring Mrk 817 on 2020-11-22 (HJD 2459175), with an approximate cadence of 1 day, aside from occasional gaps due to poor visibility from orbital pole constraints or interuptions caused by Gamma-ray Bursts or other Targets of Opportunity. For this initial period of the campaign, data were taken as part of a TOO request (PI: E. Cackett, Target IDs: 37592 and 14012 were used). Each visit is typically ∼1 ksec. The Swift XRT (Roming et al. 2005) was operated in Photon Counting mode. The UVOT (Burrows et al. 2005) was typically operated in a end-weighted filter mode (0x224c) to get exposures in all 6 UV/optical filters with a weighting of 3:1:1:1:1:2 (for UVW2 through V), with occasional use of the blue-weighted 4-filter 0x30d5 mode (3 UV filters plus U) when shorter exposures are required close to periods of pole constraints.

Swift X-ray light curves were generated using the Swift-XRT (Evans et al. 2007, 2009) data product tool[2]. All archival and new UVOT data were processed and analyzed following the procedures described by Edelson et al. (2019) and Hernández Santisteban et al. (2020), with HEASOFT version 6.28 and CALDB version 20210113. Fluxes are measured using the uvot-source tool, with a circular source extraction region of $5''$ radius and with the background measured in a surrounding $40''$–$90''$ annulus. We apply detector masks to reject data points when the source falls on regions of the chip with lower sensitivity. We follow the procedure laid out in Hernández Santisteban et al. (2020), but find that the detector masks employed there are too aggressive for the present data, eliminating many points that are consistent with the light curves to within their measurement errors. Instead, we use a more conservative set of masks defined by applying higher thresholds to the sensitivity maps, which results in eliminating 55 exposures from a total of 424.

[2] https://www.swift.ac.uk/user_objects/index.php

The Swift X-ray count rate during the campaign is significantly lower than seen previously (e.g., Morales et al. 2019). The mean $0.3 - 10$ keV count rate between $2017 - 2019$ is 0.64 c s^{-1}, while during our campaign the mean rate is 0.077 c s^{-1}, a factor of 8 lower. Despite the significant change in the X-ray count rate, the mean $UVM2$ flux is approximately same from $2017 - 2019$ as it is during our current campaign (3.88×10^{-14} vs. 3.96×10^{-14} erg s^{-1} cm^{-2} Å^{-1}). The 2017-2019 data show the X-ray and $UVM2$ rates are not correlated (Morales et al. 2019), and this continues in the current campaign.

2.6. *Ground-based photometry*

Ground-based optical imaging was obtained using the facilities listed in Table 1. These include the 2.2 m telescope at Calar Alto Observatory in Spain, the 1 m telescopes of Las Cumbres Observatory Global Telescope Network (LCO) located at McDonald Observatory in Texas, the 2 m Liverpool Telescope located on the island of La Palma in the Canary Islands, the Wise Observatory Centurion 18-inch telescope (C18) in Israel, the Yunnan Observatory 2.4 m telescope in China, and the 20-inch telescope of Dan Zowada Memorial Observatory in New Mexico. Filters included Johnson or Bessell B and V, SDSS $u'g'r'i'z'$, and Pan-STARRS z_s. Exposure times ranged from 10 s to 300 s, and at some facilities, two exposures per filter were taken on each observing night.

Basic processing steps including bias subtraction and flat-fielding were performed using the standard pipelines for each facility. For all of the data other than imaging from Calar Alto and Yunnan Observatory, photometry was carried out using an automated procedure written as a wrapper to routines in the photutils package (Bradley et al. 2020) of Astropy (Astropy Collaboration et al. 2018). The procedure automatically identifies the AGN and a set of comparison stars in each image based on the object coordinates, locates the object centroids, and then performs aperture photometry using a $5''$ aperture radius and a sky background annulus spanning 15–$20''$. Scale factors are applied to the count values in order to minimize the scatter in the comparison star light curves (separately for each telescope), and comparison star magnitudes from the APASS catalog (Henden et al. 2018) are used to calibrate the flux scale for each filter. For a given filter, data points from the same telescope and same night are combined using a weighted average. Finally, the separate light curves from each telescope are

Table 1. Ground-based Imaging Observations

Observatory/Telescope	Instrument	Filters	$N_{\rm epochs}$	References
Calar Alto 2.2m	CAFOS	V	34	
LCO 1m	Sinistro	$BV, u'g'r'i'z_{\rm s}$	80	Brown et al. (2013)
Liverpool Telescope 2m	IO:O	$u'g'r'i'z'$	5	Steele et al. (2004)
Wise Observatory 18-inch	QSI683	$g'r'i'z'$	66	Brosch et al. (2008)
Yunnan Observatory 2.4m	YFOSC	V	28	
Zowada Observatory 20-inch		$g'r'i'z_{\rm s}$	80	

intercalibrated using PyCALI[3] (Li et al. 2014), in order to account for differences in wavelength-dependent throughput. Specifically, PyCALI models light curves using a damped random walk process and applies additive and multiplicative factors to each telescope's data so as to align the fluxes into a common scale. To account for any systematic errors beyond the statistical uncertainties from the aperture photometry measurements, PyCALI also expands the error bars by adding a systematic error term in quadrature to the original uncertainties of each telescope's data. These intercalibration factors are determined in a Bayesian framework with a diffusive nested sampling algorithm (Brewer et al. 2011).

Photometry on the V-band data from Calar Alto and Yunnan Observatory was carried out with a separate software pipeline, using an aperture of radius $2''.7$ and a sky background annulus of $5''.3$–$8''.0$ for Calar Alto and an aperture radius of $5''.7$ and a background annulus spanning $11''.4$–$17''.0$ for Yunnan. These data points were merged with data from other telescopes using PyCALI to produce the final V-band light curve.

We combined the Pan-STARRS z_s and SDSS z' data together into the final z-band light curve. Given the relatively lower S/N of the z-band data (partly due to CCD fringing noise), we do not find significant differences in light curve shape or reverberation lag between these two z-band filters. In the following discussion, we will refer to the SDSS and Pan-STARRS filters as the *ugriz* bands.

2.7. *Ground-Based Optical Spectroscopy*

The coordinated program of ground-based optical spectroscopy includes observations at six observatories: the 2.2 m telescope at Calar Alto Observatory, the 2 m Faulkes Telescope North of the LCO network on Maui,

the 3 m Shane Telescope at Lick Observatory, the 2.4 m telescope at Yunnan Observatory, the 2 m Liverpool Telescope (LT), and the 2.3 m Wyoming Infrared Observatory (WIRO). Details of the instrumental setups including wavelength coverage, dispersion, slit width, and extraction aperture are listed in Table 2.

Each set of data was processed independently using standard procedures for bias subtraction, flat-field correction, and cosmic ray removal. Spectroscopic extractions and calibrations were carried out separately for each instrument, applying methods as described for each facility: Calar Alto (Hu et al. 2020); LCO (the AGN FLOYDS pipeline[4]); Lick (Silverman et al. 2012); Yunnan (Du et al. 2014); LT (the SPRAT data reduction pipeline[5]); WIRO (Brotherton et al. 2020).

Flux calibration of the spectra from Calar Alto and Yunnan was done using a comparison star observed simultaneously in the rotated slit as described by Hu et al. (2021). For data from the other telescopes, the spectra were scaled to have a constant [O III] $\lambda 5007$ emission-line intensity with the spectral fitting method described in Hu et al. (2016). For each telescope, the Hβ flux was measured by integration over the range 4951–5075 Å in the observed frame, relative to a continuum defined in the windows 4879–4930 Å and 5235–5286 Å (the 5100 Å continuum). The 5100 Å continuum and Hβ light curves from different telescopes were intercalibrated as per Equations (1) and (2) in Peterson et al. (2002) to correct for aperture effects, and then measurements with observation times closer than 0.8 days were averaged.

2.8. *Ground-Based Near-IR Spectroscopy*

In AGN STORM 1, NGC 5548 was monitored with near-IR spectroscopy two years after the main campaign (Landt et al. 2019). For AGN STORM 2 we made a point of obtaining contemporaneous NIR spectroscopy

---

[3] https://github.com/LiyrAstroph/PyCALI.

[4] https://github.com/svalenti/FLOYDS_pipeline
[5] https://telescope.livjm.ac.uk/TelInst/Inst/SPRAT

Table 2. Ground-Based Spectroscopic Observations

Telescope	Instrument	Number of Epochs	Wavelength Dispersion (Å pixel^{-1})	Wavelength Coverage (Å)	Aperture (Slit width × extraction window)
Calar Alto 2.2 m	CAFOS	34	4.47	4000–8500	$3''.0 \times 10''.6$
LCO 2 m	FLOYDS (Brown et al. 2013)	47	3.51	5400–10000	$2.0'' \times 8''.8$
			1.7	3200–5700	$2.0'' \times 8''.8$
Lick 3 m	Kast Spectrograph	7	1.0	3620–5700	$4''.0 \times 15''$
			2.6	5700–10700	$4''.0 \times 15''$
Yunnan 2.4 m	YFOSC	8	1.8	3800–7200	$2''.5 \times 8''.5$
Liverpool	SPRAT (Piascik et al. 2014)	18	4.6	4000–8000	$1''.8 \times 3''.5$
WIRO 2.3 m	Long Slit Spectrograph	62	1.49	4000–7000	$5'' \times 13''.6$
ARC 3.5 m	TripleSpec	28	1.9	9500–24600	$1''.1 \times 12''.0$
Gemini North 8 m	GNIRS	17	2.5	8500–25000	$0''.45 \times 1''.6$
IRTF 3 m	SpeX	5	2.5	7000–25500	$0''.3 \times 0''.9$

using Gemini North 8 m, ARC 3.5 m and IRTF 3 m (see Table 2). Details of these observations will be presented in a follow-up paper, but we note here that there is no evidence for absorption in the low-ionization line He I 1.08 μm (as of 2021 April 3) from either the narrow or the broad UV absorbers. This situation is very different from that of NGC 5548, which showed He I 1.08 μm absorption from both the 'obscurer' and warm absorber (Wildy et al. 2021).

3. RESULTS

3.1. *Spectral modelling*

We begin with a close examination of our highest quality observations taken on 2020-12-18 with HST and XMM-Newton. In the following section, we describe the spectral fits, which will be the baseline models for the time-resolved spectroscopy in Section 3.2, and the broadband SED and ionic column densities used for photoionization modelling in Section 3.3.

3.1.1. *The UV spectrum from 2020-12-18*

The rich set of UV absorption lines permits a detailed investigation of the properties of the absorbing gas. The many doublets and the Lyman series allow us to obtain good measurements of the ionic column densities and covering fractions due to their range in oscillator strengths.

To measure the absorption features in the HST spectra, we first model the emission spectrum. Our approach is similar to that used by Kriss et al. (2019a) in their analysis of NGC 5548 spectra from AGN STORM 1.

Our model is empirical, and although the components of the model are not strict physical representations, they enable us to separate the emission lines, the absorption features, and the continuum. Although we use an accretion disk spectrum to model the broad-band continuum of Mrk 817, to fit the far-UV spectra in detail, we approximate the 940–1750 Å continuum with a reddened powerlaw, $F_\lambda(\lambda) = F_\lambda(1000 \text{ Å})(\lambda/1000 \text{ Å})^{-\alpha}$, assuming foreground Galactic extinction with a color excess $E(B-V) = 0.022$ (Winter et al. 2011), and a ratio of selective to total extinction of $R_V = 3.1$. Although NED suggests $E(B-V) = 0.005$, we use the higher value from Winter et al. (2011) because it provides a better spectral fit. There is no indication of additional extinction in Mrk 817. All spectral components are absorbed by foreground damped Lyα by Galactic neutral hydrogen with a column density of $N(\text{H I}) = 1.15 \times 10^{20}$ cm^{-2} (Murphy et al. 1996).

For the emission lines, we use multiple Gaussian components. The brighter lines (Lyα, C IV, O VI) require four components associated with each individual multiplet, ranging from a weak narrow-line component of width ~ 500 km s^{-1} to a very broad component with width of ~ 12000 km s^{-1}. Weaker lines such as P V, Si II, and C II require only a single broad component.

We use negative flux Gaussian profiles to model the intrinsic absorption components. Single narrow Gaussians with a full-width at half-maximum of FWHM$\sim$ 150 km s^{-1} model the narrow absorption lines well. For the broad absorption troughs, we permit these Gaussians to be asymmetric with different dispersions on the
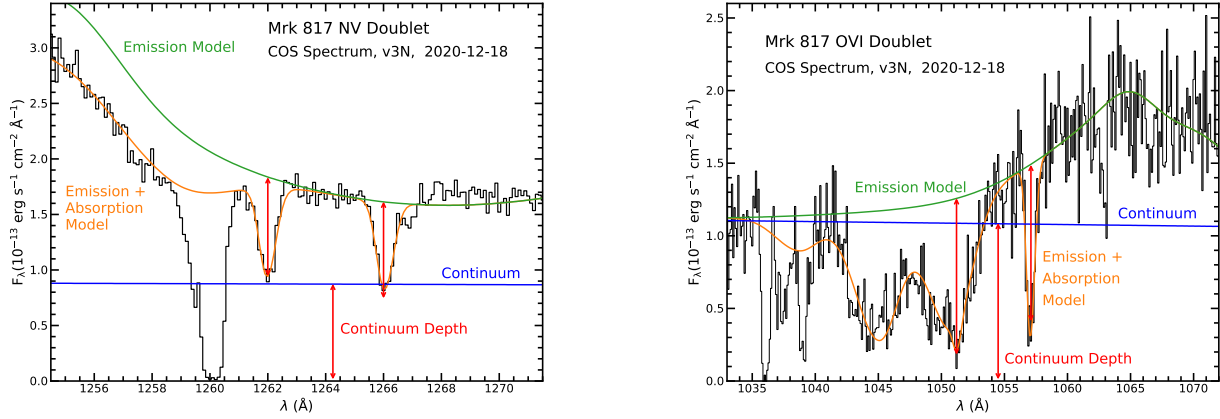
Figure 4. *Left:* COS spectrum of the region surrounding the N V absorption doublet in Mrk 817 from 2020-12-18 (black). The data are binned by 8 pixels (∼1 resolution element) and are plotted as a function of observed wavelength. The best-fit emission model is in green, and the best-fit model including both broad and narrow absorption is in orange. The model continuum is in blue. The red arrow represents the continuum depth, and we compare it to the depths of both the blue and the red transitions as measured from the total emission model. Note that the blue line has the same depth as the continuum, but that the red line is slightly shallower. The deep trough bluewards of N V is due to foreground interstellar lines: Si II 1260.42Å (strongest line) and S II 1259.52Å (weak dip on the blue side). *Right:* Same as left, but for the region surrounding the broad and narrow O VI absorption doublets. Both the blue and the red transitions have the same depth as the continuum, indicating saturation and full coverage of the continuum emission.

blue and red sides of the profile, i.e. for a line centered at λ_c, the Gaussian dispersion for $\lambda > \lambda_c$ is $\sigma_{\rm red}$, and for $\lambda < \lambda_c$ it is $\sigma_{\rm blue}$. The ratio of the dispersions is a free parameter. The broad troughs in Mrk 817 tend to have a rounded triangular profile with the deepest point of the trough on the blue side and a more extensive wing on the red side. Their widths range from $\sim 1000 - 1500$ km s^{-1}. Note that this is not a physical description for the absorbing gas. Deriving physical information (e.g. column densities and covering fractions) requires making further assumptions on the origin of the velocity profile of an absorption trough and on which elements of the emission model are actually covered by the absorbing gas.

The narrow absorption lines are simple, resolved, and symmetric. Aside from O VI they appear to be unsaturated. The broad absorption troughs are more complex. They appear to be fully saturated, with profiles determined by variations in the covering factor as a function of velocity. Deep troughs like Lyα, C IV, O VI, and S VI have almost exactly the same asymmetric profile shape–steeper on the blue side, shallower on the red side. Even lines of low abundance elements like P V have doublet ratios of ∼1:1, and so are saturated, even when the line has a lot equivalent width. We point readers to Appendix Table 5 for a summary of the equivalent width (EW) and other empirical properties of the narrow and broad absorption lines from observations on 2020-12-18.

To determine whether the absorbing gas in each case covers all the emission (e.g. lines and continuum), or just the continuum, or fractions of each, we look in detail at the narrow N V and O VI doublets. Fig. 4-*left* shows that the red transition of the N V doublet is deeper than the blue transition. However, our full emission model (that accounts for the broad N V absorption trough) shows that, compared to the unabsorbed overlying emission, the blue transition is indeed slightly deeper. In fact, it has exactly the same depth as the continuum. Although this is not a definitive interpretation, it implies that the narrow emission covers only the continuum and not the broad-line emission.

Similarly, Fig. 4-*right* illustrates the same behavior for O VI. In this case the blue transition of the O VI doublet falls within the red trough of the broad O VI absorption. At first glance, the red transition of the doublet again appears deeper than the blue, but when the depth of the blue line is measured relative to the full emission model, we see that both lines are consistent with saturation at full coverage of only the continuum. The residual emission below the bottom of the blue line equals the modeled intensity of the overlying broad-line emission as if that emission is unabsorbed.

Similar arguments apply to the broad O VI absorption troughs. Relative to the continuum emission, they both have the same depth. However, that depth is shallower than the continuum strength, indicating that the broad

lines are saturated, but that they only partially cover the continuum.

We do not show the same level of detail for C IV, Si IV, P V, or S VI, but Fig. 2 shows that the regions surrounding these doublets are strongly dominated by continuum emission. We therefore measure column densities assuming that both the broad and narrow absorption lines cover only the continuum emission.

For S VI the depths of the blue and red transitions have close to a 2:1 ratio and appear to be nearly optically thin. The broad absorption troughs in S VI have equal depths and appear to be nearly saturated, but they only partially cover the continuum. Like S VI, the broad troughs in C IV and P V appear to be saturated, and only partially cover the continuum. Si IV shows only broad absorption troughs. The red transition in Si IV is shallower than the blue, indicating that the doublet is unsaturated. This yields a reliable measure of both the column density and the covering factor using the doublet method of Barlow & Sargent (1997).

Table 6 gives our measurements of the ionic column densities for both the narrow and the broad absorption troughs, using the apparent optical depth (AOD) method of Savage & Sembach (1991). We assume they both only cover the continuum and not the overlying broad line emission. For the narrow absorption lines, we assume that the covering factor is 100%, $f_c = 1$, and uniform in velocity. For each line we give a best measured value, and quote a 2σ lower limit ($\Delta\chi^2 = 3.82$) from the best-fit χ^2 value or the value from direct integration of the line profile normalized by the continuum emission, whichever is lower. Upper limits are also reported at 2σ ($\Delta\chi^2 = 3.82$).

Just as the Si IV doublet appears to be unsaturated, the highest order Lyman lines are also unsaturated, giving us a well constrained series solution for the H I column density. Lyα is highly saturated, with its profile determined by covering factor. Assuming the same profile shape for the higher-order lines, we fit the series in a consistent way. Measuring column densities independently for each line using these fitted profiles and assuming the same covering factor as a function of velocity, $f_c(v)$, as derived for Lyα gives consistent H I column densities as shown in Table 7.

For singlets like C III* λ1176, C III λ977 and N III λ991, we again assume their broad absorption troughs are saturated. We use the shape of Lyα to determine their profiles and assume that the trough shape determines the covering factor as a function of velocity, $f_c(v)$. To measure the column density, N_{ion}, we integrate the line profile using $f_c(v)$ from Lyα and assume an optical depth of $\tau = 4.5$ at its deepest point, which corresponds
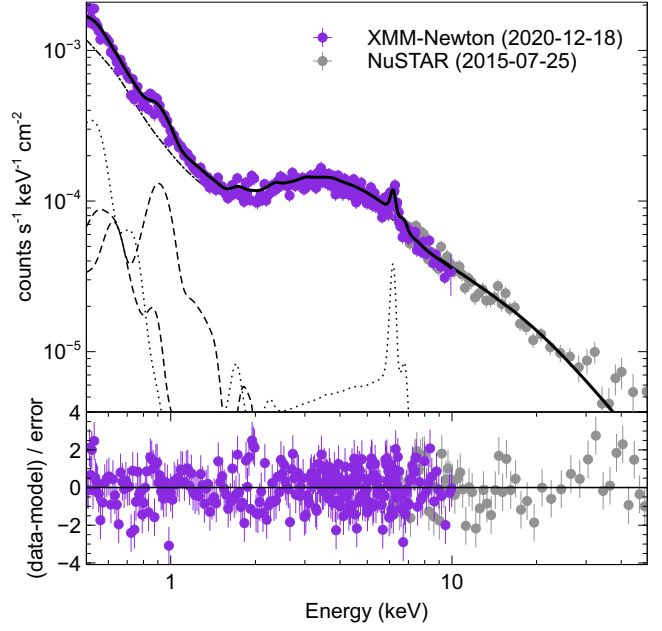

Figure 5. The XMM-Newton spectrum from 2020-12-18 (purple) and archival NuSTAR spectrum, overlaid with the best fit model described in Table 3 (black solid line). The model consists of several components: emission from the inner accretion flow (a Comptonization continuum and relativistic reflection) that is absorbed by the new ionized obscurer (black dot-dash line); distant reflection fitting the narrow iron K line (dotted line); and photoionized emission from two zones of circumnuclear gas (dashed lines).

to a $\sim 1\%$ residual intensity. (Given the high degree of saturation, these column densities could be even higher.)

For blended multiplets like C III* λ1176, N III λ991, and C IV λ λ1548,1550, we sum the oscillator strengths to convert the optical depth to a column density. Given the high degree of saturation in many lines, column densities could be even higher. However, the unsaturated Si IV doublet and the unsaturated higher order Lyman lines, Lyγ and Lyδ, give secure column density measurements.

3.1.2. *The X-ray spectrum from 2020-12-18*

As indicated in Fig. 3, at the beginning of the AGN STORM 2 campaign, Mrk 817 was in a deep X-ray low flux state. Compared to the archival XMM-Newton and NuSTAR observations, most of the changes are in soft X-rays. This fact, together with the sudden appearance of broad UV absorption lines (including from low-abundance elements like phosphorous), lead us to the conclusion that the X-ray variability is largely due to obscuration of the central compact source.

There are sharp features in the X-ray spectrum below 1 keV that do not vary between the XMM-Newton

spectrum and lowest flux NICER spectrum from 2021-01-20, despite significant diversion at higher energies. This suggests emission from distant circumnuclear gas that responds on long timescales. To probe further, we examine the high-resolution RGS data covering the 10–36Å (0.35–1.2 keV) range. We fit the continuum with a phenomenological powerlaw + blackbody model (though more complex/physical models do not change the results). There are clear indications of emission lines from O VIII Lyα, O VII triplet, N VII, C VI radiative recombination continuum (RRC), and C VI at longer wavelengths. These can be well fit in SPEX (Kaastra et al. 1996, 2020) with two PION photoionization models (Mehdipour et al. 2016a), where the velocity broadening was fixed to $\sigma = 400\,\mathrm{km\,s^{-1}}$. Using the O VIII Ly$\alpha$ line (and confirmed by comparison with N VII and O VII resonance line), we measure an outflow velocity of $v = -400 \pm 70\,\mathrm{km\,s^{-1}}$. We fix the outflow velocity of the PION models at this value, and fix the density of the slab to 1 cm^{-3}, as it does little to influence the line flux. The most important difference between these two components is their ionization parameters. Given the quality of our data, we cannot distinguish between the covering factor, Ω, and the column density, as both a higher column density and larger covering factor lead to an increase in line strength. The best fit column densities, ionization parameters and covering factors for these two components can be found in Table 3. The RGS data will be the subject of follow-up papers. For now we simply use the results to inform our fitting of the lower-resolution broadband spectra (Fig. 5).

We fit the CCD spectra in XSPEC (Arnaud 1996). For the soft photoionized emission lines (dashed black lines; Fig. 5), we used a pre-computed and simplified table version of PION, called PION_XS (Parker et al. 2019). The grid assumes that the ionization continuum is a powerlaw spectrum with $\Gamma = 2$, typical of AGN and appropriate for this source. The PN data are most sensitive to the ionization parameters, and so we freeze them to the best fit values from the RGS analysis. There is also a clear detection of a narrow neutral iron Kα line, which we fit with the XILLVER model (García & Kallman 2010), with the log of the ionization parameter fixed at 0 (dotted black line; Fig. 5). We model the continuum as a cutoff powerlaw ($E_\mathrm{cut} = 300$ keV) absorbed by a partial covering ionized absorber (ZXIPCF in XSPEC; Reeves et al. 2008). This resulted in an adequate fit ($\chi^2/\mathrm{dof} = 1451/1413$). Similarly good fits and parameter estimates are found when using the SPEX model PION, which properly accounts for the ionizing continuum. The addition of a soft excess component below

Table 3. X-ray spectrum model parameters

Component	Parameter	Value
tbabs	N_H ($10^{22}\mathrm{cm}^{-2}$)	0.01^{c}
zxipcf	N_H ($10^{22}\mathrm{cm}^{-2}$)	$6.95^{+0.8}_{-0.7}$
	$\log\xi$ (erg·cm·s^{-1})	$0.55^{+0.3}_{-0.4}$
	Cov. Frac. Ω	$0.93^{+0.01}_{-0.008}$
relxillD	index	> 6.6
	a_*	> 0.97
	i (degrees)	< 40
	Γ	$1.91^{+0.04}_{-0.09}$
	$\log\xi$ (erg·cm·s^{-1})	$2.7^{+0.2}_{-0.3}$
	A_Fe	6^{+3}_{-2}
	$\log N_\mathrm{e}$ (cm^{-3})	$18.7^{p}_{-0.6}$ ^{b}
	reflection fraction	$0.3^{+0.3}_{-0.2}$
PION	$\log\xi$ (erg·cm·s^{-1})	2.7 ± 0.3^{a}
	N_H ($10^{21}\mathrm{cm}^{-2}$)	7.6^{a}
	Cov. Frac. Ω	0.02^{a}
PION	$\log\xi$ (erg·cm·s^{-1})	1.5 ± 0.2 ^{a}
	N_H ($10^{21}\mathrm{cm}^{-2}$)	50.6^{a}
	Cov. Frac. Ω	0.011^{a}
XMM-Newton	χ^2/d.o.f.	1083/1109
NuSTAR	χ^2/d.o.f.	353/314

[a] Parameter fit to RGS spectrum and fixed for PN analysis

[b] Pegged to maximum value of $\log N_\mathrm{e} = 10^{19}$ cm^{-3}

[c] Fixed parameter

1 keV improves the fit at the 3σ level. In the literature, the soft excess has often been modeled as a 'warm corona' (e.g., COMPTT in XSPEC; Petrucci et al. 2013), or as relativistically broadened reflection (e.g., RELXILLD; Dauser et al. 2010). In favor of the reflection interpretation, García et al. (2019) argue that the optically-thick warm corona would produce a spectrum substantially different from a blackbody with electron scattering due to atomic absorption, and such features are not observed in AGN. Our spectrum of Mrk 817 cannot statistically differentiate between these models ($\chi^2/\mathrm{dof} = 1436/1409$ using the COMPTT model and $\chi^2/\mathrm{dof} = 1437/1409$ for the RELXILLD model). We choose to proceed with the relativistic reflection model here, and in Sections 3.2 and 3.3. Most importantly, we see that the choice of soft excess model does not affect the inferred properties of the ionized obscurer. The final model in XSPEC syntax is: TBABS*(PION_XS+ PION_XS + XILLVER + ZXIPCF*(RELXILLD)). See Table 3 for details of the fit.

Finally, we tested a very different scenario where instead of an ionized obscurer, the low flux state was caused by an intrinsically low-flux corona, where the corona is extremely close to the black hole and light bending effects cause most of the photons to either fall into the black hole or irradiate the inner ($\sim 2\ r_{\rm g}$) accretion disk. Such a model has successfully explained the spectra and reverberation time lags of highly variable narrow-line Seyfert 1 AGN (e.g., 1H 0707-495; Fabian et al. 2012 or IRAS 13224-3809; Kara et al. 2013; Alston et al. 2020). This model does provide a reasonable fit to the XMM-Newton data ($\chi^2/{\rm dof} = 1118/1109$), but overpredicts the NuSTAR flux, and the joint XMM-Newton and NuSTAR fit is poor. Moreover, in such a scenario, the newly discovered broad absorption troughs in the UV would not be due to a new obscuration event, but instead due to changes in the ionizing continuum. This is challenging to reconcile with observations of low-abundance species like phosphorous, which point instead to a high column density gas. Because of this and the statistical evidence of the X-ray fit, we do not consider this model further.

3.2. *The evolution of the ionized obscurer*

The HST and XMM-Newton observations presented above represent just one day of the year-long AGN STORM 2 campaign. Here we use the models presented above as the baseline for fitting the daily UV HST and NICER X-ray observations to track the evolution of the obscurer.

The XMM-Newton spectral decomposition discussed in Section 3.1.2 provided constraints on the column density, ionization and covering factor of the ionized absorber that obscures the X-ray source. We use the best fit model in Section 3.1.2 as the baseline model, and freeze parameters that should not display inter-day variability (e.g., elemental abundances, black hole spin, emission from parsec-scale gas and beyond), and only allow the ionized absorber parameters (column density, ionization parameter, covering fraction) and continuum parameters (powerlaw photon index and normalization) to vary. To constrain these parameters, we needed to increase the signal to noise by binning the NICER data into 7 epochs, each now with $\sim 5 - 10$ ks of data. In the first 40 days of the campaign, the X-ray flux decreased by over an order of magnitude. Our time-resolved spectral analysis shows that this is largely driven by changes in the hydrogen column density of the ionized absorber (see Fig. 6).

We compare the X-ray absorber evolution to the broad P V absorption line EW and ionizing continuum in Fig. 6. The same trend in EW and ionizing continuum is
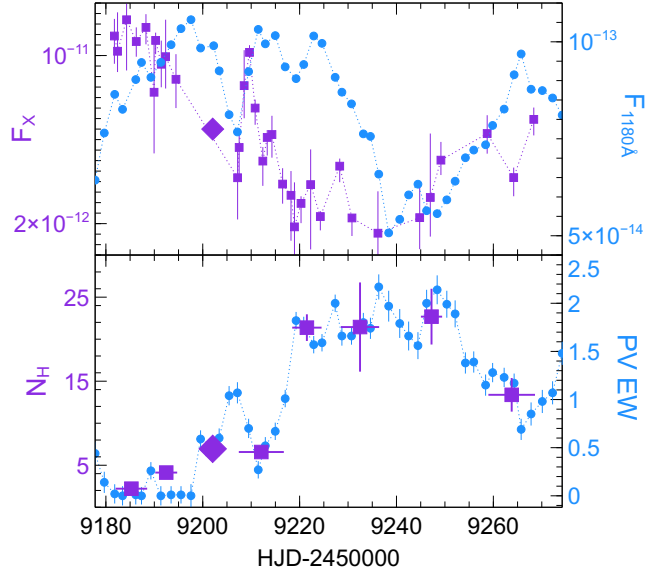

Figure 6. Comparison of X-ray and UV absorption during the first third of the AGN STORM 2 campaign. The top panel shows the NICER 0.3-10 keV flux in units of erg cm^{-2} s^{-1} (purple) compared to the 1180 Å flux (erg cm^{-2} s^{-1} Å^{-1}) measured by HST (blue). The purple diamond demarcates the XMM-Newton observation (also in 0.3-10 keV range). The bottom panel shows the column density of the X-ray obscurer in units of 10^{22} cm^{-2} (purple), overlaid with equivalent width of the broad P V absorption trough in units of Å (blue).

seen in all of the broad absorption troughs of lower ionization, lower abundance species, including P V, C III* and Si IV. The bottom panel of Fig. 6 shows a clear correlation between the column density measured in X-rays and the strength of the broad absorption trough.

3.3. *Photoionization Modeling*

To constrain the location and composition of the absorber producing the narrow and broad UV absorption lines shown in Section 3.1.1, we used Cloudy photoionization models. The ionization and thermal equilibrium in a photoionized plasma is dependent on the spectral energy distribution (SED) of the ionizing source. To construct a model for the ionizing SED, we fit the HST COS+STIS spectrum and the accompanied XMM-Newton observation taken in 2020-12-18.

3.3.1. *The ionizing SED*

To model the NIR to UV continuum (Fig. 7), we used a disk blackbody component (DBB in SPEX), which provides a good fit to the continuum of the STIS+COS spectrum for a maximum temperature $T_{\rm max} = 20$ eV. This model is based on a geometrically thin, optically
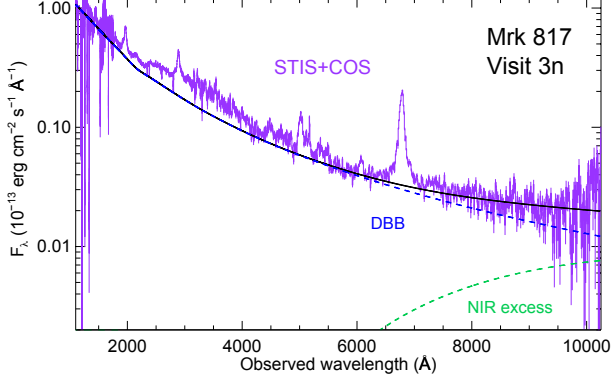
Figure 7. NIR-optical-UV spectrum, taken with HST COS and STIS on 2020-12-18. The continuum is fitted with a disk blackbody (DBB; dashed blue line). The NIR excess is modeled with a simple blackbody component (dashed green line) and may be attributed to thermal emission from the hottest regions of the dusty torus. The excess emission above the DBB continuum in the 2000–5500 Å range is the complex Fe II and Balmer continuum emission, which we exclude in our fitting of the continuum. The total best-fit continuum model is shown in solid black line, which is reddened with $E(B-V) = 0.022$.
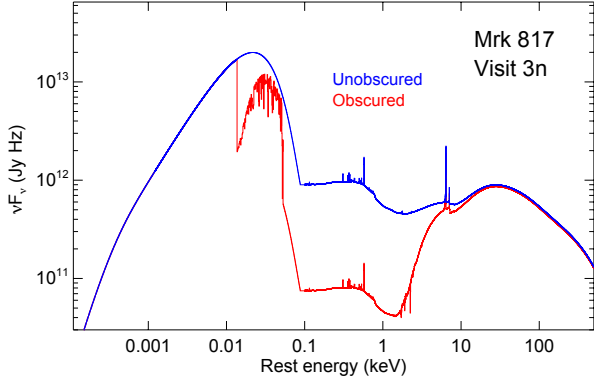
Figure 8. SED model of Mrk 817, before and after adding absorption by the obscuring gas. The unobscured SED (blue) has a luminosity of 1.1×10^{45} erg s^{-1} ($L/L_{\rm Edd} = 22\%$), and the obscured (red) has 6.7×10^{44} erg s^{-1}.

thick, Shakura-Sunyaev accretion disk. Reddening was accounted for in the same way as in Section 3.1.1. We observe an excess of emission above the DBB continuum over the 2000–5500 Å range, typical of the Fe II and Balmer continuum emission of most AGN. This is notoriously challenging to model accurately, and so we exclude this emission feature in our fitting of the continuum. In order to obtain a good fit to the optical-UV continuum with the DBB model, we find that we are left with some excess emission in the NIR above the DBB

continuum at > 7000 Å. We attempted different models for this excess emission. We tested the various bulge and host galaxy starlight template models of Kinney et al. (1996). However, such starlight models over-predict the 5500–6000 Å continuum observed in the STIS spectrum. We find the NIR excess is best modeled as the short wavelength Wien tail from the hottest regions of the dusty torus. We thus used a simple blackbody component for this excess emission. The presence of such a torus contribution in the NIR is also supported by the 2MASS J, H, K_s fluxes that are reported in NED (the 'profile-fit' values of Skrutskie et al. 2006). While a Wien tail is our favored description, we cannot rule out other origins of this blackbody component (e.g. diffuse continuum emission Chelouche et al. 2019; Netzer 2020). Regardless, it does not affect our photoionization modeling.

The model for the X-ray to EUV spectrum is based on results presented in Section 3.1.2, where the soft excess is fit by relativistic reflection off the inner accretion disk (see Section 3.1.2 for details). We also consider photoionization models that assume a warm corona soft excess (similar to the SED assumed in Mehdipour et al. 2015), and find essentially the same solution. The ionized absorber is modeled with PION in SPEX because it extends down to the Lyman limit. The parameter constraints are similar to those found with zx-IPCF in earlier sections: $N_{\rm H} = 9.6 \pm 0.6 \times 10^{22}$ cm^{-2}, $\log \xi = 1.0 \pm 0.6$ (erg cm s^{-1}) and covering fraction $\Omega = 0.92 \pm 0.01$. The 1–1000 Ryd ionizing luminosities are 6.3×10^{44} erg s^{-1} (for the unobscured SED) and 2.4×10^{44} erg s^{-1} (obscured SED). The resulting obscured and unobscured SED models are shown in Fig. 8.

3.3.2. *The Narrow Absorption Line Solution*

We used Cloudy v17.02 (Ferland et al. 2017) to determine the photoionization structure of the outflowing gas producing the narrow absorption lines in the HST spectra (Section 3.1.1). We tried using the obscured and unobscured SEDs shown in Fig. 8. The ionic column densities are computed with Cloudy over a grid of total column density $N_{\rm H}$ and ionization parameter ξ. The ionization parameter ξ (Krolik et al. 1981) is defined as $\xi = L / n_{\rm H} r^2$ (in units of erg cm s^{-1}), where L is the luminosity of the ionizing source over 1–1000 Ryd, $n_{\rm H}$ is the hydrogen density, and r is the distance between the gas and the ionizing source.

We set the elemental abundances to the proto-solar values of Lodders et al. (2009). We also tried the default abundances of Cloudy (Ferland 2006). The results from these two sets of abundances are similar.
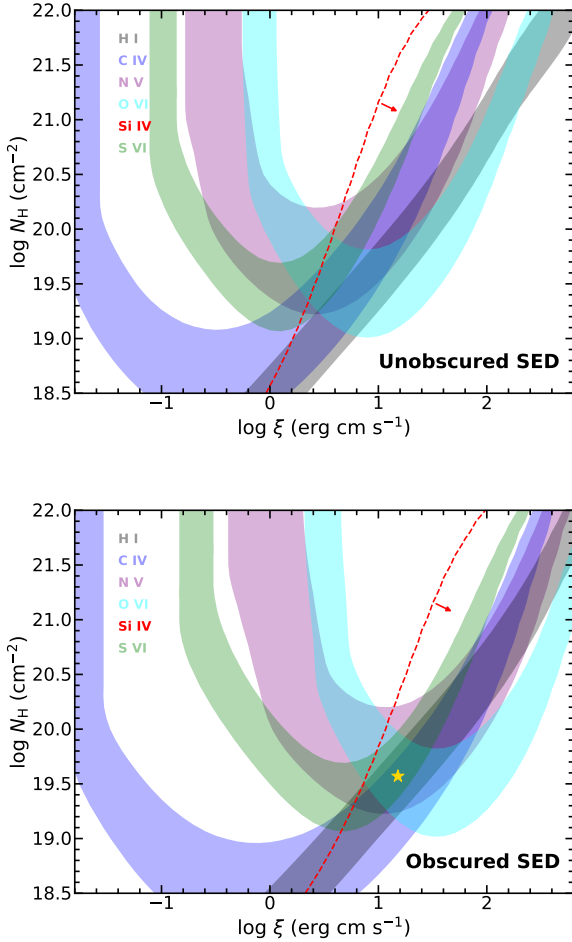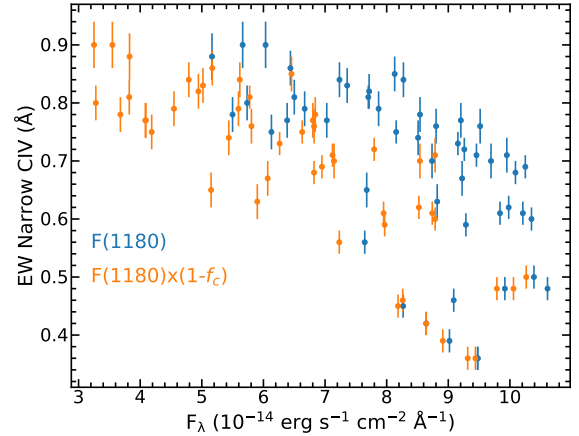
Figure 10. Observed correlation between the equivalent width of narrow C IV $\lambda1548$ absorption and the continuum flux at 1180 Å, F(1180) (blue points). Orange points show how the correlation is improved by inferring an obscured continuum flux by attenuating the observed flux by the transmission of the deepest point in the C III* absorption trough, $1 - f_c$.

Figure 9. Photoionization model constraints on the narrow UV absorber in Mrk 817, calculated using the unobscured (*top panel*) and obscured (*bottom panel*) SEDs from the 2020-12-18 observation. The colored bands encompass the measured column density of each ion and its associated uncertainty. The dashed line for Si IV represents an upper-limit. Allowed photoionization solution would lie in a region where bands of all ions overlap. For the obscured SED case, there is a valid solution region at around $\log N_{\rm H}\,({\rm cm}^{-2}) = 19.5$ and $\log \xi \,({\rm erg\ cm\ s}^{-1}) = 1$, indicated with a gold star.

Fig. 9 shows the results for the narrow UV absorbers as observed on 2020-12-18. The calculations are done with the unobscured SED in the top panel, and with the obscured SED in the bottom panel. The column density constraints for each ion are shown by colored bands, and a good solution is one where the bands overlap. Encouragingly, Fig. 9 shows that there is no solution for the unobscured SED, while there is a solution for the obscured one at around $\log N_{\rm H}\,({\rm cm}^{-2}) = 19.5$ and $\log \xi \,({\rm erg\ cm\ s}^{-1}) = 1$ (Fig. 9-bottom panel). This suggests that the obscuring gas is located interior to the UV narrow-line absorber.

This hypothesis is corroborated by the empirical result that the changes in the narrow absorption line equivalent width correlate better with the obscured continuum than the unobscured continuum (see Fig. 10). The obscured continuum is estimated by scaling the observed flux by the transmission fraction derived from the C III* broad absorption trough. For the unobscured continuum, the Pearson correlation coefficient and p-value are -0.61 and 2.6×10^{-6}, respectively, while for the obscured continuum these are -0.81 and 6.7×10^{-13}.

3.3.3. *The Broad Absorption Line Solution*

Here we use the 2020-12-18 observations to determine the ionization structure of the gas producing the broad UV absorption troughs. First we determine the hydrogen number density ($n_{\rm H}$) by measuring the electron number density (n_e) using the C III* absorption trough where in a fully ionized plasma $n_e \approx 1.2 n_{\rm H}$. The ratio of column densities between each level of the C III* multiplet and the C III ground state is sensitive to n_e and the temperature T (see Gabel et al. 2005; Arav et al. 2015). To measure n_e we modeled the observed troughs with Gaussians (corresponding to the six C III* transitions). We used the CHIANTI atomic database (CHIANTI 10.0) to model the ratios of the different excited states from $\log n_e = 3$ [cm^{-3}] to $\log n_e = 13$ [cm^{-3}]. In order to determine the depth of the individual troughs, an estimate for the total column density of C III was needed as well. The optical depths of the individual
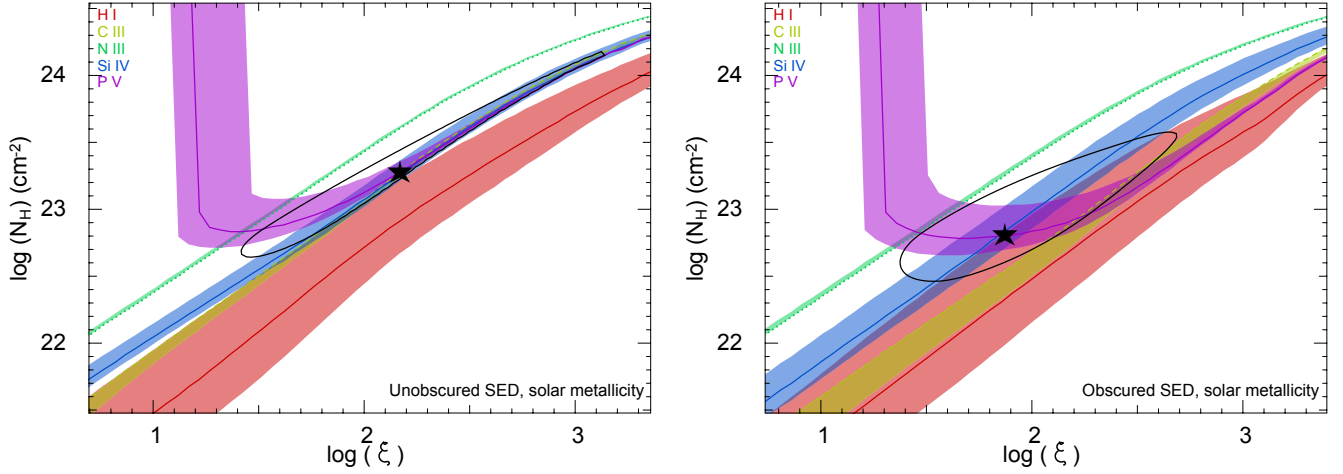
Figure 11. $\log N_H$ vs $\log \xi$ for the unobscured (*left*) and obscured (*right*) SED models. The ions in the outflow system, represented by the colored bands, provide constraints on N_H and ξ in the form of upper and lower limits, as well as measurement values, of measured column densities. Dotted lines are upper limits, dashed lines are lower limits, and solid lines are measurements. The uncertainty in the column density measurements are represented by the shaded bands. The solution found with χ^2 minimization is represented by the black star, and the 1σ is represented by a black ellipse.

troughs are

$$\tau_i = \frac{N_{\text{C III}} f_i \lambda_i}{3.8 \times 10^{14} \text{ cm}^{-2}} \times \frac{r_i}{\sqrt{2\pi}\sigma_v} \qquad (1)$$

where $N_{\text{C III}}$ is the total column density of C III, f_i is the oscillator strength, r_i is the ratio between the excited state and the total C III column densities, and σ_v is the Gaussian velocity width space determined by using the Lyman α absorption trough as a template. The troughs were modeled assuming apparent optical depth. We find that $\log n_e = 10.5^{+0.8}_{-0.5}$ (in units of cm^{-3}) best fits the trough of C III*, with the errors determined through adjusting n_e so that the χ^2 increases by 1.

Similar to the previous section, using the obscured and unobscured SEDs in Fig. 8 and using the hydrogen number densities as computed above, we produced grids of Cloudy models with $\log N_H$ (units cm^{-2}) ranging from 20 to 25.5, and $\log \xi$ ranging from 0.5 to 3.5, and search for the parameters that lead to ionic column densities closest to the measured values. Fig. 11 shows the solution found with the unobscured SED (*left*) and obscured SED (*right*). The obscured solution meets all the ionic column density constraints and therefore is a viable physical model. The solution region (indicated by the black star in the ellipse) lies at roughly at $\log N_H (\text{cm}^{-2}) = 22.8$ and $\log \xi = 1.9$, which is formally higher than that found from X-ray spectral modelling ($\log \xi \sim 1$, Section 3.1.2). This is likely explained by differences in the photoionization codes/models (as described in Mehdipour et al. 2016a).

Finally, for completeness, and motivated by previous work showing AGN with super-solar metallicity outflows (Gabel et al. 2006; Arav et al. 2007), we created a grid of models with higher metallicity by applying the element ratios of Ballero et al. (2008), using the recipe of Miller et al. (2020) for five times solar metallicity ($Z_\odot$). Raising the metallicity shifted the position of the H I band relative to the other elements, and provides a slightly better solution compared to that found at solar metallicity.

3.4. Early reverberation mapping results

Next we present RM results of the first 97 days of the Mrk 817 campaign. The continuum RM results are given in Section 3.4.1 and the emission-line RM results in Section 3.4.2.

For both continuum and line reverberation, we calculate lags using the standard linear interpolation cross-correlation (ICCF) approach with uncertainties estimated from the flux randomization, random subset sampling technique (as implemented by Peterson et al. 2004). In this approach a large number of realizations (here we use $N = 10,000$) of the light curves are created through resampling of the data. In each realization the flux of each data point is randomized assuming a Gaussian distribution with a mean and standard deviation equal to the measured flux and its 1σ uncertainty. In addition, the light curve is randomly sampled with replacement, meaning that some points are selected multiple times while others are not selected at all. Those that are selected multiple times have their errors weighted ap-

propriately. For each realization we measure the cross-correlation function (CCF) and its centroid value. The lag is then taken as the median of the CCF centroid distribution, and its 1σ uncertainty from the 16 and 84% quantiles.

3.4.1. *Continuum disk Reverberation Mapping*

We tested using several bands as the reference light curve. The HST 1180 Å light curve has the highest variability amplitude, however, it resulted in a poor peak correlation coefficient ($R_{\max}$) with the longer wavelength optical bands. For instance, it gives an $R_{\max}$ of approximately 0.1 with the z band. The g band light curve has the largest number of data points, but a significantly lower variability amplitude than the UV light curves. While it gave the best-constrained optical ground-based lags, the UV lags were significantly more poorly constrained. The Swift/$UVW2$, on the other hand, has an excellent balance between the number of data points (nearly twice that of the HST 1180Å light curve), high variability amplitude and good correlations with all wavebands. We therefore use this as the reference band against which we measure the lags.

The resulting rest-frame lags are given in Table 4. We also give the fractional variability amplitude, F_{var} (Vaughan et al. 2003), which is largest in the UV and decreases with wavelength, and the maximum correlation coefficient $R_{\max}$. The right-hand panels of Fig. 12 show the CCFs (solid lines) and the CCF centroid distributions, while Fig. 13 shows the lags as a function of wavelength. The lags increase with wavelength, approximately following $\tau \propto \lambda^{4/3}$, as expected for a standard Shakura & Sunyaev thin disk (Cackett et al. 2007). We fit $\tau = \tau_0 \left[(\lambda/\lambda_0)^{\beta} - y_0 \right]$, with $\lambda_0 = 1869$ Å (the rest-frame wavelength of the $UVW2$ band), and $\beta = 4/3$, and where y_0 allows the fit to be non-zero at λ_0. This gives a best-fitting value of $\tau_0 = 1.01 \pm 0.09$ days.

In the disk reprocessing scenario the lags should scale with black hole mass, M, and Eddington ratio, $\dot{m}_{\mathrm{E}}$ following $\tau \propto M^{2/3} \dot{m}_{\mathrm{E}}^{1/3}$. Comparing to NGC 5548 (Fausnaugh et al. 2016b) we assume $M_{\mathrm{NGC5548}} = 5 \times 10^7$ M$_\odot$, and $\dot{m}_{\mathrm{E,NGC5548}} = 0.05$ and for Mrk 817 $M_{\mathrm{Mrk817}} = 3.85 \times 10^7$ M$_\odot$, and $\dot{m}_{\mathrm{E,Mrk817}} = 0.2$. Given these values we expect $\tau_{0,\mathrm{NGC5548}}/\tau_{0,\mathrm{Mrk817}} = 0.75$. Adjusting the best-fitting $\tau \propto \lambda^{4/3}$ to the NGC 5548 continuum lags to have the same reference wavelength as we use here we get $\tau_{0,\mathrm{NGC5548}} = 0.64$ days. Therefore, the observed ratio of $\tau_{0,\mathrm{NGC5548}}/\tau_{0,\mathrm{Mrk817}} = 0.63$ is consistent with the expected mass and Eddington ratio scaling given the uncertainties.

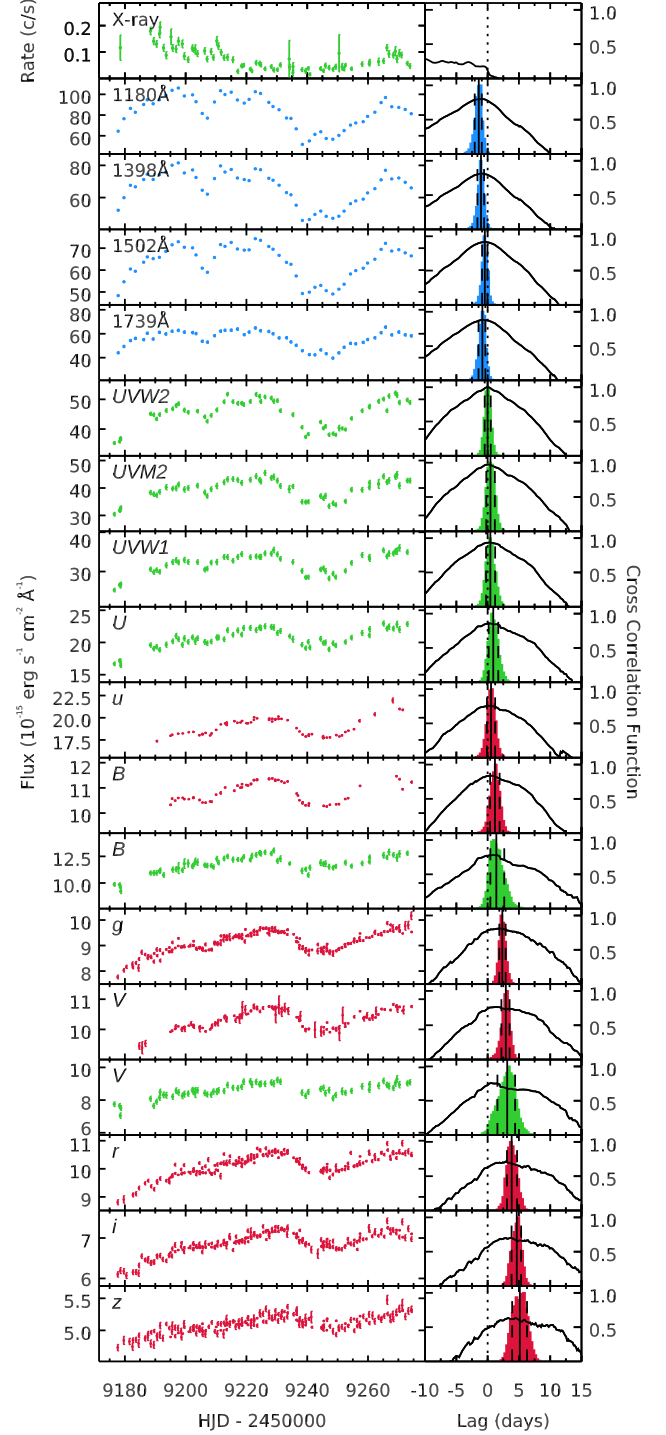Recent analytical models for accretion disk lags have been developed using transfer functions calculated from

Figure 12. *Left:* Mrk 817 continuum light curves from HST (blue), Swift (green) and ground-based telescopes (red). All fluxes have units of 10^{-15} erg s^{-1} cm^{-2} Å^{-1}, aside from the *Swift* $0.3 - 10$ keV X-ray light curve which is shown as a count rate. *Right:* Solid black lines show the cross-correlation function with respect to the Swift $UVW2$ band. Colored histograms show the ICCF centroid lag distributions, while the vertical solid and dashed lines give the lag and 1σ uncertainty range.

general-relativistic ray-tracing simulations (Kammoun et al. 2021a,b). We fit these models assuming both a non-spinning ($a = 0$) and a maximally spinning ($a = 0.998$) black hole. We fix the black hole mass at $M = 3.85 \times 10^7$ M$_\odot$, and use the unabsorbed 2 – 10 keV X-ray flux from the XMM observations of 8.5×10^{-12} erg s^{-1} cm^{-2}. We leave the mass accretion rate and the height of the X-ray source, h, as free parameters in the fit, but, following Kammoun et al. (2021b) we constrain h to be between 2.5 and 100 R_G. Both the $a = 0$ and $a = 0.998$ models fit the data equally well, and we find that the height of the X-ray source is unconstrained. We get best-fitting mass accretion rates of $\dot{m}_{\rm Edd} = 0.06^{+0.07}_{-0.02}$ and $\dot{m}_{\rm Edd} = 0.32^{+0.39}_{-0.12}$ for $a = 0$ and $a = 0.998$ respectively. The best-fitting $a = 0.998$ model is shown as a dashed line in Fig. 13.

All previous intensive campaigns that utilized Swift and ground-based monitoring (Edelson et al. 2019; Cackett et al. 2018; Vincentelli et al. 2021; Hernández Santisteban et al. 2020) have found significant (typically a factor of ~ 2) excess lags in u/U bands, relative to the adjacent bands or to the fits. By contrast, the lags presented here from the first $\sim 1/3$ of the campaign show no evidence of excess u/U band lags. In the one source, NGC 4593, where spectroscopic observations covering this wavelength range were available, Cackett et al. (2018) showed that this u/U band excess was, in fact, a broad excess leading up to the Balmer jump. This has been associated with lags from the diffuse continuum arising in the BLR gas (Korista & Goad 2001, 2019; Lawther et al. 2018; Chelouche et al. 2019; Netzer 2020). We will continue to monitor the u/U band lags to better understand under what conditions this feature is or is not present.

Despite the strong and variable absorption observed in the X-rays and the UV absorption lines and the lack of an X-ray/UV correlation, the UV and optical continuum variability and continuum lags look very similar to what would be expected. Either the disk sees a different source of irradiating photons than the X-rays we observe (e.g., the X-ray absorber is not located between the X-ray and UV/optical continuum region or does not block all lines of sight between those regions), or a different mechanism drives variability in the disk (e.g. corona-heated accretion disk reprocessing; Sun et al. 2020a,b).

3.4.2. Broad-line region reverberation mapping

The broad-line region reverberation mapping traces larger (centi-parsec) scales around the black hole. In order to probe these larger scales, the optical spectroscopy campaign began before the HST/Swift/NICER cam-
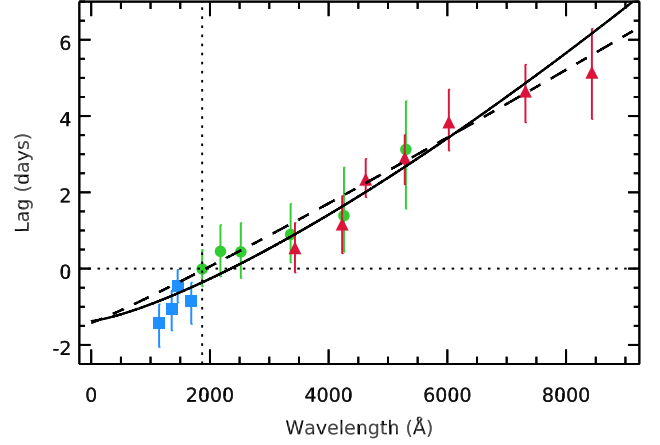

Figure 13. Continuum lags (rest-frame) calculated with respect to the *Swift/UVW2* band. Data from *HST*, *Swift* and ground-based telescopes are shown as blue squares, green circles, and red triangles respectively. The solid line shows the best-fitting $\tau \propto \lambda^{4/3}$ relation. The dashed line is the best-fitting model using the relations in Kammoun et al. (2021a), with a maximal black hole spin.

Table 4. Continuum lags and light curve properties

Filter	Telescope	$F_{\rm var}$	$R_{\rm max}$	Lag
				(days)
1180Å	HST	0.177	0.80	$-1.42^{+0.48}_{-0.64}$
1398Å	HST	0.155	0.81	$-1.06^{+0.46}_{-0.57}$
1502Å	HST	0.119	0.92	-0.46 ± 0.43
1739Å	HST	0.121	0.88	$-0.84^{+0.48}_{-0.61}$
UVW2 (1928Å)	Swift	0.103	1.00	0.00 ± 0.50
UVM2 (2246Å)	Swift	0.090	0.97	$0.45^{+0.69}_{-0.66}$
UVW1 (2600Å)	Swift	0.078	0.94	$0.44^{+0.76}_{-0.69}$
U (3465Å)	Swift	0.071	0.86	$0.90^{+0.81}_{-0.73}$
u (3540Å)	Ground	0.051	0.76	0.55 ± 0.65
B (4361Å)	Ground	0.036	0.84	$1.17^{+0.74}_{-0.77}$
B (4392Å)	Swift	0.065	0.78	$1.39^{+1.27}_{-0.95}$
g (4770Å)	Ground	0.043	0.82	$2.34^{+0.54}_{-0.48}$
V (5448Å)	Ground	0.035	0.77	$2.91^{+0.60}_{-0.70}$
V (5468Å)	Swift	0.048	0.76	$3.12^{+1.27}_{-1.56}$
r (6215Å)	Ground	0.036	0.72	$3.84^{+0.86}_{-0.76}$
i (7545Å)	Ground	0.037	0.70	$4.65^{+0.70}_{-0.83}$
z (8700Å)	Ground	0.025	0.63	$5.15^{+1.14}_{-1.23}$

paign. In Fig. 14-*top*, we show the 5100Å continuum light curve (red) and the Hβ light curve (dark red). The panel on the right shows the results of the ICCF analysis, searching for correlations over -10 to 50 days (1/3 of the duration of the light curve). The peak of the cross-
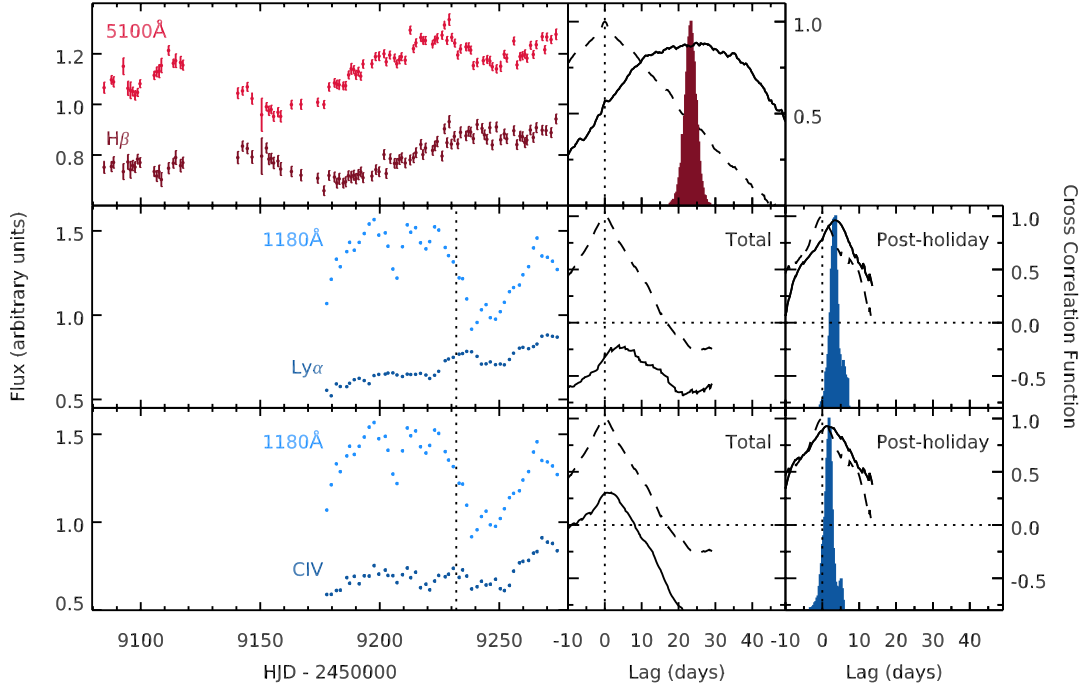
Figure 14. The broad line region lags from the AGN STORM 2 campaign to date. (*Top:*) The 5100 Å continuum (red) and the Hβ light curve (dark red). The panel on the right shows the cross correlation function (CCF; the solid black line) between these two bands, while the dashed line shows the auto correlation function (ACF) of the continuum. The colored histogram is the ICCF centroid lag distributions, resulting in an Hβ lag of 23.2 ± 1.6 days (rest frame) behind the continuum. (*Middle, Bottom:*) The 1180 Å continuum (blue) and the Lyα light curve (dark blue; *middle*) and C IV (*bottom*). The panels immediately to the right of the light curves show the CCF (solid line) and ACF (dashed line) of the entire campaign. We notice from the light curves that the correlation is much greater at HJD> 2459232. We show the CCF and ACF and ICCF lag distribution for this 'post-holiday' period in the far right panels. The resulting in time lags are $\tau_{\mathrm{Ly}\alpha} = 3.3^{+1.5}_{-1.2}$ days and $\tau_{\mathrm{C\ IV}} = 1.8^{+1.2}_{-1.3}$ days. We emphasize that these BLR lags are calculated from a subset of our data and will be updated as the campaign continues.

correlation coefficient is high ($R_{\max}$=0.89), and the time lag is measured to be 23.2 ± 1.6 days (rest frame). The time lags were also measured using JAVELIN (Zu et al. 2011), and the time lag was consistent ($22.0^{+2.0}_{-1.4}$ days). This is consistent with previous 5100Å vs. Hβ lags measured for this source from previous campaigns (Zu et al. 2011).

Thanks to the dedicated HST campaign, we can also measure the UV broad line lags. The light curves for Lyα and C IV are shown in the middle and bottom panels of Fig. 14, and ACFs, CCFs and ICCF lag distributions are shown in the panels immediately to the right (labeled 'total'). Again, we search for correlations over a time-frame that is 1/3 the duration of the light curve. Calculating the CCF for the total campaign thus far, we found little to no correlation between the UV lines and the 1180 Å continuum. This is indicated by the solid black line cross correlation functions that peak at $R_{\max} = -0.2$ and $R_{\max} = 0.3$ for Lyα and C IV respectively. These correlations are so low that we cannot determine a lag.

However, we notice a change, starting at HJD=2459232, when the UV lines *do* begin to correlate with the continuum. The panels on the far right show the ACFs, CCFs and ICCF lag distributions from HJD=2459232 and beyond (labeled 'post-holiday'). The post-holiday light curves show $R_{\max}$ of nearly unity (0.96 for Lyα and 0.93 for C IV), and we measure the lags to be $\tau_{\mathrm{Ly}\alpha} = 3.3^{+1.5}_{-1.2}$ days and $\tau_{\mathrm{C\ IV}} = 1.8^{+1.2}_{-1.3}$ days (rest frame). We emphasize that this period of correlated variability spans only 43 days, a small subset of our total campaign, and so the lags should be regarded as preliminary. Further measurements including velocity-resolved reverberation mapping and updated black hole mass estimates will be carried out using data from the full duration of the campaign.

4. DISCUSSION

In the canonical reverberation mapping paradigm, the variability we observe is thought to be driven by rapid variability in the X-ray corona. This driving light curve irradiates other gas flows, and those light echoes across different wavebands allow us to map out scales from

the inner edge of the accretion disk (e.g., Zoghbi et al. 2010; Kara et al. 2016), to the outer accretion disk (e.g., Shappee et al. 2014; Edelson et al. 2015; Cackett et al. 2018) to the broad line region (Peterson et al. 2004; Bentz et al. 2013). While much of this paradigm has been successful in explaining the variability and time delays observed in dozens of Seyfert 1 AGN, there are important exceptions, that fundamentally can teach us more about the complex nature and dynamics of gas flows around supermassive black holes. For instance, variable line of sight obscuration (e.g., Zoghbi et al. 2019; Dehghanian et al. 2019), variability due to mass accretion rate fluctuations in the disk (e.g., McHardy et al. 2014) or variability in the geometry of the corona (e.g., Alston et al. 2020) are not included in the simplest reverberation paradigm, but indeed, are likely important for understanding the entire system.

Understanding when and why the simple paradigm works or does not work requires large spectroscopic and photometric multi-wavelength efforts spanning a range of timescales that allow us to put the AGN's variability into context. This is the goal of the AGN STORM 2 campaign, where we have consolidated efforts from across many AGN fields in order to get a complete picture of the Seyfert galaxy Mrk 817. When the campaign began in November 2020, we discovered Mrk 817 in a never-before-seen obscured state, with a depressed soft X-ray flux (Fig. 3) and broad UV absorption troughs (Fig. 2) suggesting that an ionized, dust-free absorber located at the inner broad line region partially obscures our line of sight to the central engine.

The obscuration strongly affects the soft X-ray flux (Fig. 6), which, naively, one might think explains the lack of correlation between X-rays and longer wavelengths (Fig. 12). However, earlier Swift monitoring of Mrk 817 (when the source was not obscured) also show little correlation between X-rays and longer wavelengths (Morales et al. 2019). Moreover, this lack of correlation is commonly seen in other AGN that do not exhibit time-variable obscuration (Buisson et al. 2017; Edelson et al. 2019), and thus likely points to additional complexities in the coupling between the accretion disk and the corona. Despite a lack of correlation between the observed driving light curve (X-rays) and longer wavelengths, we still observe UV and optical continuum lags as expected from a thin disk being irradiated and heated by a compact ionizing source (Fig. 13). In future work with the complete dataset, we will also test models including a diffuse continuum from the broad line region that may contribute to the continuum lags.

The standard reverberation mapping paradigm also explains the 23-day time lag between the 5100 Å con-

tinuum light curve and the Hβ light curve as due to the light travel time between the accretion disk and BLR (Fig. 14-top). This lag agrees well with the radius-luminosity relation (Bentz et al. 2013). That said, the UV lines like Lyα and C IV are more complicated, as the first 55 days (before HJD 2459232) show a much weaker correlation between continuum and the C IV broad emission line than later epochs (Fig. 14-$bottom$). The $\sim 2-3$ day lags of the UV lines are much shorter than the Hβ lags, and in fact, are comparable to the lags between UV and the NIR continuum, which may suggest that the UV broad line region and the outer accretion disk are co-spatial. Future work modelling the reverberation lags will put better constraints on the geometry and dynamics of the accretion disk and broad line region, but for reference, 1 light-day corresponds to a distance of 455 GM/c^2 in units of gravitational radii.

A de-coupling of the UV continuum and broad emission lines was seen also in the AGN STORM 1 campaign in NGC 5548 for a period of 60–70 days (Goad et al. 2016). Because the anomalous period was more exaggerated in the higher ionization lines (like C IV and Si IV) than in lower ionization lines like Lyα, Goad et al. (2016) suggested that the de-coupling was due to a depletion of ionizing photons above $E > 56$ eV, relative to those near 13.6 eV. This could either be caused by intrinsic changes in the X-ray corona or due to line-of-sight obscuration. In the case of Mrk 817, the UV holiday occurs at the beginning of the campaign, as X-ray emission was becomes more obscured, and the strength of the broad UV absorption troughs increases (Fig. 6). Then, as the line-of-sight obscuration decreases, we measure coherent lags between the UV continuum and broad emission lines. This may suggest that obscuration effects are responsible for the de-coupling of continuum and UV broad lines. As the campaign continues, we will be able to better measure time lags associate with the various broad emission lines.

From the first third of the AGN STORM 2 Campaign targeting Mrk 817, we have identified and characterized a new ionized obscurer. With an ionizing luminosity of 2.4×10^{44} erg s^{-1} for the obscured SED, our measurement of an electron number density of log $n_e = 10.5$, and the best fit ionization parameter of $\log \xi = 1.9$, the UV absorbing gas in the obscurer lies at a radius of $R = 3.7^{+0.9}_{-1.1}$ light days. This location is consistent with the inner BLR, which, from our preliminary reverberation lag analysis, we suggest is ~ 3 light-days ($\sim 1500 \ GM/c^2$) from the black hole. Continuum reverberation lags also suggest that the accretion disk extends out this far (and beyond), and so we suggest that

the ionized obscurer is associated with an accretion disk wind.

Similar accretion disk wind models have been envoked to explain the changes to the broadband SED (Mehdipour et al. 2016b), high ionization absorption lines (Kriss et al. 2019b) and the broad line region holiday in NGC 5548 (Dehghanian et al. 2019, 2020). In such a model, the equatorial accretion disk wind is densest at the base and more diffuse at larger scale heights. Some numerical simulations of disk winds, especially of radiation driven disk winds (e.g., Murray et al. 1995; Proga et al. 2000; Proga 2007), also show that the wind base can be a crucial site of line emission and absorption, and can affect broad line reverberation lags (e.g., Chiang & Murray 1996; Proga & Kallman 2004; Kashi et al. 2013; Waters et al. 2016; Giustini & Proga 2019). Comparisons between theoretical models and observations will be presented in future work.

In the case of Mrk 817, it is possible that at the very beginning of the campaign, a lower density, larger scale height wind component is present, and accounts for modest X-ray and UV light-of-sight obscuration. The base of the wind, however, is dense enough to interfere with UV BLR irradiation. As the campaign continues through HJD 2459232, the dense wind flows outwards, and the line-of-sight obscuration increases (as shown in Fig. 6). With the ejection of the densest part of the wind, the BLR can again 'see' the accretion disk, and the UV BLR reverberation ensues. As the gas reservoir of the wind is depleted, the line-of-sight obscuration decreases from HJD 2459232 onwards. This unveiling of the central source will have important implications for future observations later on in the campaign, allowing us to put this model to the test.

5. SUMMARY AND CONCLUSIONS

To summarize, our major findings from the first third of the AGN STORM 2 campaign of Mrk 817 (November 2020–March 2021) are as follows:

- Compared to archival observations from 2019, the soft X-ray flux dropped by a factor of ~ 10. This variability suggests the presence of a partially covering, ionized obscurer.

- The UV continuum did not drop relative to archival observations, but the HST spectra revealed new blueshifted absorption lines.

- Analysis of the narrow N V doublet and the broad O VI doublet reveal that the broad and narrow absorbers cover only the continuum emission, and therefore likely originate at the inner BLR or within.

- The photoionization solution for the narrow and broad absorption UV lines is most self-consistently explained if the ionizing SED is obscured. This is supported by the fact that the narrow absorption lines correlate better with a continuum that is obscured by the broad absorption component.

- Disk continuum lags: The UV/optical continuum lags (on the order of days) are consistent with a centrally illuminated Shakura-Sunyaev thin accretion disk, which may suggest that the absorber may be beyond the inner accretion disk.

- Optical broad line region lags: The Hβ emission line lags the optical continuum by 23 days, similar to previous Hβ reverberation mapping campaigns of this source.

- UV broad line region lags: The first 55 days of the campaign showed little correlation between the UV continuum and UV broad lines like Lyα and C IV but from the next 42 days (as the obscuration appears to decrease), we measure UV BLR lags of 2-3 days.

We continue to monitor Mrk 817 across the electromagnetic spectrum. At the time of writing, the X-ray flux is increasing and the broad UV absorption lines are decreasing in equivalent width, perhaps suggesting that we are entering a new, unobscured phase of the campaign.

APPENDIX

A. SUMMARY OF UV LINE CHARACTERISTICS

To characterize the absorption lines more quantitatively, we can empirically measure the centroid of an absorption feature to obtain the mean outflow velocity, its full-width at half maximum (FWHM), and its Equivalent Width (EW; integrated normalized flux). Table 5 summarizes these properties for the narrow and broad absorption lines in Mrk 817 for Visit 3N.

Table 6 shows the column densities of the UV narrow and broad absorption lines that were used for the photoionization modelling in Section 3.3.

Details of the H I column densities can be found in Table 7.

REFERENCES

Table 5. Absorption Line Properties in Mrk 817 Visit 3N

Line	λ_{rest}	v_{out}[a]	FWHM[b]	EW[c]	f_c[d]
	km s^{-1}	km s^{-1}	Å		
Narrow Absorption Lines					
S VI	933.38	−3722	79	0.20 ± 0.07	0.70
S VI	944.52	−3722	79	0.13 ± 0.07	0.46
O VI	1031.93	−3709	219	0.84 ± 0.13	1.00
O VI	1037.62	−3709	219	0.84 ± 0.13	1.00
Lyα	1215.67	−3709	219	0.56 ± 0.02	0.58
N V	1238.82	−3726	161	0.66 ± 0.04	0.91
N V	1242.80	−3726	161	0.66 ± 0.04	0.90
C IV	1548.19	−3722	173	0.69 ± 0.05	0.71
C IV	1550.77	−3722	173	0.56 ± 0.05	0.58
Broad Absorption Lines					
S VI	933.38	−5591	922	1.78 ± 0.37	0.57
S VI	944.52	−5591	922	1.70 ± 0.37	0.55
N III	990.68	−5510	1165	0.36 ± 0.406	0.087
C III	977.02	−5510	1165	0.51 ± 0.344	0.124
O VI	1031.93	−5510	1165	3.46 ± 0.26	0.79
O VI	1037.62	−5510	1165	3.39 ± 0.26	0.77
P V	1117.98	−5510	1165	0.56 ± 0.03	0.12
P V	1128.01	−5510	1165	0.55 ± 0.03	0.12
C III*	1175.74	−5510	1165	0.66 ± 0.022	0.133
Lyα	1215.67	−5561	1165	3.03 ± 0.027	0.59
N V	1238.82	−5510	1165	1.57 ± 0.12	0.30
N V	1242.80	−5510	1165	1.50 ± 0.12	0.28
Si IV	1393.76	−5476	911	0.81 ± 0.05	0.18
Si IV	1402.77	−5476	911	0.71 ± 0.05	0.16
C IV	1548.19	−5479	1353	3.29 ± 0.15	0.44
C IV	1550.77	−5479	1353	2.96 ± 0.15	0.40

[a] Outflow velocities are relative to a systemic redshift of 0.0031455 (Strauss & Huchra 1988). The uncertainty is dominated by systematic errors at 5 km s^{-1}.

[b] Full width at half maximum

[c] Equivalent width relative to the continuum flux.

[d] Maximum possible covering fraction as measured at the deepest point of the absorption trough.

Alston, W. N., Fabian, A. C., Kara, E., et al. 2020, Nature Astronomy, 4, 597

Arav, N., Gabel, J. R., Korista, K. T., et al. 2007, ApJ, 658, 829

Arav, N., Chamberlain, C., Kriss, G. A., et al. 2015, A&A, 577, A37

Arnaud, K. A. 1996, in Astronomical Society of the Pacific Conference Series, Vol. 101, Astronomical Data Analysis Software and Systems V, ed. G. H. Jacoby & J. Barnes, 17

Astropy Collaboration, Price-Whelan, A. M., Sipőcz, B. M., et al. 2018, AJ, 156, 123

Table 6. Absorption Line Column Densities in Mrk 817 Visit 3N

Ion	Best-fit log N_{ion}	log N_{ion} Lower Limit	N_{ion} Upper Limit
	(cm^{-2})	(cm^{-2})	(cm^{-2})
Narrow Absorption Lines			
S VI	14.00	13.64	14.27
O VI	15.58	15.33	16.13
H I	14.09	14.00	14.64
N V	14.79	14.69	14.84
C IV	14.41	14.35	14.47
Broad Absorption Lines			
S VI	15.95	15.28	16.00[a]
N III	16.48	10.00	16.54
C III	16.04	10.00	16.10
O VI	16.82	16.57	16.89[a]
P V	16.02	15.88	16.29
C III*	15.91	15.90	15.91
H I	16.20	15.81	16.55
N V	16.68	15.00	16.98[a,b]
Si IV	15.81	15.64	16.06
C IV	16.58	15.75	16.86[a]

[a] Upper limit could be much higher due to the high level of saturation.

[b] Highly uncertain due to blending with the Lyα emission-line profile.

Table 7. H I Column Densities from Broad Lyman Lines in Mrk 817 Visit 3N

Lyman Line	Best-fit N_{HI}	AOD N_{HI} [a]	N_{HI} Upper Limit
	(10^{16} cm^{-2})	(10^{16} cm^{-2})	(10^{16} cm^{-2})
Lyα	2.00	0.047	2.02
Lyβ	0.90	0.14	2.00
Lyγ	1.40	0.36	3.51
Lyδ	1.60	0.60	4.89

[a] Apparent Optical Depth as calculated from a direct integration of the normalized line profile as described by Savage & Sembach (1991).

Ballero, S. K., Matteucci, F., Ciotti, L., Calura, F., & Padovani, P. 2008, A&A, 478, 335

Barlow, T. A., & Sargent, W. L. W. 1997, AJ, 113, 136

Bentz, M. C., Peterson, B. M., Netzer, H., Pogge, R. W., & Vestergaard, M. 2009, ApJ, 697, 160

Bentz, M. C., Denney, K. D., Grier, C. J., et al. 2013, ApJ, 767, 149

Blandford, R. D., & McKee, C. F. 1982, ApJ, 255, 419

Bradley, L., Sipőcz, B., Robitaille, T., et al. 2020, astropy/photutils: 1.0.0, doi:10.5281/zenodo.4044744

Brewer, B. J., Pártay, L. B., & Csányi, G. 2011, Statistics and Computing, 21, 649

Brosch, N., Polishook, D., Shporer, A., et al. 2008, Ap&SS, 314, 163

Brotherton, M. S., Du, P., Xiao, M., et al. 2020, ApJ, 905, 77

26

Brown, T. M., Baliber, N., Bianco, F. B., et al. 2013,
  PASP, 125, 1031
Buisson, D. J. K., Lohfink, A. M., Alston, W. N., & Fabian,
  A. C. 2017, MNRAS, 464, 3194
Burrows, D. N., Hill, J. E., Nousek, J. A., et al. 2005,
  SSRv, 120, 165
Cackett, E. M., Chiang, C.-Y., McHardy, I., et al. 2018,
  ApJ, 857, 53
Cackett, E. M., Horne, K., & Winkler, H. 2007, MNRAS,
  380, 669
Chelouche, S., Trache, D., Tarchoun, A. F., & Khimeche,
  K. 2019, Journal of Energetic Materials, 37, 387
Chiang, J., & Murray, N. 1996, ApJ, 466, 704
Croton, D. J., Springel, V., White, S. D. M., et al. 2006,
  MNRAS, 365, 11
Dashtamirova, D., & Fischer, W. 2020, Cosmic Origins
  Spectrograph Instrument Handbook, Version 12.1, Tech.
  rep., STScI, Baltimore
Dauser, T., Wilms, J., Reynolds, C. S., & Brenneman,
  L. W. 2010, MNRAS, 409, 1534
De Rosa, G., Peterson, B. M., Ely, J., et al. 2015, ApJ, 806,
  128
Dehghanian, M., Ferland, G. J., Kriss, G. A., et al. 2019,
  ApJ, 877, 119
—. 2020, ApJ, 898, 141
Dehghanian, M., Ferland, G. J., Peterson, B. M., et al.
  2021, ApJ, 906, 14
Du, P., Hu, C., Lu, K.-X., et al. 2014, ApJ, 782, 45
Dunn, J. P., Jackson, B., Deo, R. P., et al. 2006, PASP,
  118, 572
Ebrero, J., Kriss, G. A., Kaastra, J. S., & Ely, J. C. 2016,
  A&A, 586, A72
Edelson, R., Gelbord, J. M., Horne, K., et al. 2015, ApJ,
  806, 129
Edelson, R., Gelbord, J., Cackett, E., et al. 2019, ApJ, 870,
  123
Evans, P. A., Beardmore, A. P., Page, K. L., et al. 2007,
  A&A, 469, 379
—. 2009, MNRAS, 397, 1177
Event Horizon Telescope Collaboration, Akiyama, K.,
  Alberdi, A., et al. 2019, ApJL, 875, L6
Fabian, A. C., Zoghbi, A., Wilkins, D., et al. 2012,
  MNRAS, 419, 116
Fausnaugh, M. M., Denney, K. D., Barth, A. J., et al.
  2016a, ApJ, 821, 56
—. 2016b, ApJ, 821, 56
Ferland, G. J. 2006, Hazy, A Brief Introduction to Cloudy
  06.02
Ferland, G. J., Chatzikos, M., Guzmán, F., et al. 2017,
  RMxAA, 53, 385

Ferrarese, L., & Merritt, D. 2000, ApJL, 539, L9
Gabel, J. R., Arav, N., & Kim, T. 2006, ApJ, 646, 742
Gabel, J. R., Kraemer, S. B., Crenshaw, D. M., et al. 2005,
  ApJ, 631, 741
García, J., & Kallman, T. R. 2010, ApJ, 718, 695
García, J. A., Kara, E., Walton, D., et al. 2019, ApJ, 871,
  88
Gardner, E., & Done, C. 2017, MNRAS, 470, 3591
Gebhardt, K., Bender, R., Bower, G., et al. 2000, ApJL,
  539, L13
Gehrels, N., Chincarini, G., Giommi, P., et al. 2004, ApJ,
  611, 1005
Giustini, M., & Proga, D. 2019, A&A, 630, A94
Goad, M. R., Korista, K. T., De Rosa, G., et al. 2016, ApJ,
  824, 11
GRAVITY Collaboration, Sturm, E., Dexter, J., et al.
  2018, Nature, 563, 657
GRAVITY Collaboration, Amorim, A., Bauböck, M., et al.
  2021, arXiv e-prints, arXiv:2102.00068
Green, J. C., Froning, C. S., Osterman, S., et al. 2012, ApJ,
  744, 60
Henden, A. A., Levine, S., Terrell, D., et al. 2018, in
  American Astronomical Society Meeting Abstracts, Vol.
  232, American Astronomical Society Meeting Abstracts
  #232, 223.06
Hernández Santisteban, J. V., Edelson, R., Horne, K., et al.
  2020, MNRAS, 498, 5399
Hopkins, P. F., Hernquist, L., Cox, T. J., & Kereš, D. 2008,
  ApJS, 175, 356
Horne, K., Peterson, B. M., Collier, S. J., & Netzer, H.
  2004, PASP, 116, 465
Horne, K., De Rosa, G., Peterson, B. M., et al. 2021, ApJ,
  907, 76
Hu, C., Wang, J.-M., Ho, L. C., et al. 2016, ApJ, 832, 197
Hu, C., Li, Y.-R., Du, P., et al. 2020, ApJ, 890, 71
Hu, C., Li, S.-S., Yang, S., et al. 2021, ApJS, 253, 20
Kaastra, J. S., & Bleeker, J. A. M. 2016, A&A, 587, A151
Kaastra, J. S., Mewe, R., & Nieuwenhuijzen, H. 1996, in
  UV and X-ray Spectroscopy of Astrophysical and
  Laboratory Plasmas, 411–414
Kaastra, J. S., Raassen, A. J. J., de Plaa, J., & Gu, L.
  2020, SPEX X-ray spectral fitting package,
  doi:10.5281/zenodo.3939056
Kaastra, J. S., Kriss, G. A., Cappi, M., et al. 2014a,
  Science, 345, 64
—. 2014b, Science, 345, 64
Kammoun, E. S., Dovčiak, M., Papadakis, I. E.,
  Caballero-García, M. D., & Karas, V. 2021a, ApJ, 907, 20
Kammoun, E. S., Papadakis, I. E., & Dovčiak, M. 2021b,
  MNRAS, arXiv:2103.04892

Kara, E., Alston, W. N., Fabian, A. C., et al. 2016, MNRAS, 462, 511

Kara, E., Fabian, A. C., Cackett, E. M., et al. 2013, MNRAS, 428, 2795

Kashi, A., Proga, D., Nagamine, K., Greene, J., & Barth, A. J. 2013, ApJ, 778, 50

Kinney, A. L., Calzetti, D., Bohlin, R. C., et al. 1996, ApJ, 467, 38

Korista, K. T., & Goad, M. R. 2001, ApJ, 553, 695

—. 2019, MNRAS, 489, 5284

Kriss, G. A. 2001, in Astronomical Society of the Pacific Conference Series, Vol. 224, Probing the Physics of Active Galactic Nuclei, ed. B. M. Peterson, R. W. Pogge, & R. S. Polidan, 45

Kriss, G. A., De Rosa, G., Ely, J., et al. 2019a, ApJ, 881, 153

Kriss, G. A., Lee, J. C., Danehkar, A., et al. 2018, ApJ, 853, 166

Kriss, G. A., De Rosa, G., Ely, J., et al. 2019b, ApJ, 881, 153

Krolik, J. H., McKee, C. F., & Tarter, C. B. 1981, ApJ, 249, 422

Landt, H., Ward, M. J., Kynoch, D., et al. 2019, MNRAS, 489, 1572

Lawther, D., Goad, M. R., Korista, K. T., Ulrich, O., & Vestergaard, M. 2018, MNRAS, 481, 533

Li, Y.-R., Wang, J.-M., Hu, C., Du, P., & Bai, J.-M. 2014, ApJL, 786, L6

Lodders, K., Palme, H., & Gail, H.-P. 2009, Landolt Börnstein, 44

Longinotti, A. L., Krongold, Y., Kriss, G. A., et al. 2013, ApJ, 766, 104

Mathur, S., Gupta, A., Page, K., et al. 2017, ApJ, 846, 55

McHardy, I. M., Cameron, D. T., Dwelly, T., et al. 2014, MNRAS, 444, 1469

Mehdipour, M., Kaastra, J. S., & Kallman, T. 2016a, A&A, 596, A65

Mehdipour, M., Kaastra, J. S., Kriss, G. A., et al. 2015, A&A, 575, A22

—. 2016b, A&A, 588, A139

—. 2017, A&A, 607, A28

Miller, J. M., Zoghbi, Z., Reynolds, M. T., et al. 2021, arXiv e-prints, arXiv:2103.09789

Miller, T. R., Arav, N., Xu, X., Kriss, G. A., & Plesha, R. J. 2020, ApJS, 247, 41

Morales, A. M., Miller, J. M., Cackett, E. M., Reynolds, M. T., & Zoghbi, A. 2019, ApJ, 870, 54

Murphy, E. M., Lockman, F. J., Laor, A., & Elvis, M. 1996, ApJS, 105, 369

Murray, N., Chiang, J., Grossman, S. A., & Voit, G. M. 1995, ApJ, 451, 498

Netzer, H. 2020, MNRAS, 494, 1611

Parker, M. L., Pinto, C., Fabian, A. C., et al. 2017, Nature, 543, 83

Parker, M. L., Longinotti, A. L., Schartel, N., et al. 2019, MNRAS, 490, 683

Pei, L., Fausnaugh, M. M., Barth, A. J., et al. 2017, ApJ, 837, 131

Peterson, B. M. 1993, PASP, 105, 247

Peterson, B. M., Berlind, P., Bertram, R., et al. 2002, ApJ, 581, 197

Peterson, B. M., Ferrarese, L., Gilbert, K. M., et al. 2004, ApJ, 613, 682

Petrucci, P. O., Paltani, S., Malzac, J., et al. 2013, A&A, 549, A73

Piascik, A. S., Steele, I. A., Bates, S. D., et al. 2014, in Society of Photo-Optical Instrumentation Engineers (SPIE) Conference Series, Vol. 9147, Ground-based and Airborne Instrumentation for Astronomy V, ed. S. K. Ramsay, I. S. McLean, & H. Takami, 91478H

Pounds, K. A., King, A. R., Page, K. L., & O'Brien, P. T. 2003, MNRAS, 346, 1025

Proga, D. 2007, in Astronomical Society of the Pacific Conference Series, Vol. 373, The Central Engine of Active Galactic Nuclei, ed. L. C. Ho & J. W. Wang, 267

Proga, D., & Kallman, T. R. 2004, ApJ, 616, 688

Proga, D., Stone, J. M., & Kallman, T. R. 2000, ApJ, 543, 686

Reeves, J., Done, C., Pounds, K., et al. 2008, MNRAS, 385, L108

Roming, P. W. A., Kennedy, T. E., Mason, K. O., et al. 2005, SSRv, 120, 95

Savage, B. D., & Sembach, K. R. 1991, ApJ, 379, 245

Shakura, N. I., & Sunyaev, R. A. 1973, A&A, 500, 33

Shappee, B. J., Prieto, J. L., Grupe, D., et al. 2014, ApJ, 788, 48

Silverman, J. M., Foley, R. J., Filippenko, A. V., et al. 2012, MNRAS, 425, 1789

Skrutskie, M. F., Cutri, R. M., Stiening, R., et al. 2006, AJ, 131, 1163

Starkey, D., Horne, K., Fausnaugh, M. M., et al. 2017, ApJ, 835, 65

Steele, I. A., Smith, R. J., Rees, P. C., et al. 2004, in Society of Photo-Optical Instrumentation Engineers (SPIE) Conference Series, Vol. 5489, Ground-based Telescopes, ed. J. Oschmann, Jacobus M., 679–692

Strauss, M. A., & Huchra, J. 1988, AJ, 95, 1602

Sun, M., Xue, Y., Brandt, W. N., et al. 2020a, ApJ, 891, 178

Sun, M., Xue, Y., Guo, H., et al. 2020b, ApJ, 902, 7

Tombesi, F., Cappi, M., Reeves, J. N., et al. 2010, A&A, 521, A57

Uttley, P., Cackett, E. M., Fabian, A. C., Kara, E., & Wilkins, D. R. 2014, A&A Rv, 22, 72

Vaughan, S., Edelson, R., Warwick, R. S., & Uttley, P. 2003, MNRAS, 345, 1271

Vincentelli, F. M., McHardy, I., Cackett, E. M., et al. 2021, MNRAS, arXiv:2104.04530

Waters, T., Kashi, A., Proga, D., et al. 2016, ApJ, 827, 53

Wildy, C., Landt, H., Ward, M. J., Czerny, B., & Kynoch, D. 2021, MNRAS, 500, 2063

Williams, P. R., Pancoast, A., Treu, T., et al. 2020, ApJ, 902, 74

Winter, L. M., Danforth, C., Vasudevan, R., et al. 2011, ApJ, 728, 28

Woodgate, B. E., Kimble, R. A., Bowers, C. W., et al. 1998, PASP, 110, 1183

Yu, Q., & Tremaine, S. 2002, MNRAS, 335, 965

Zoghbi, A., Fabian, A. C., Uttley, P., et al. 2010, MNRAS, 401, 2419

Zoghbi, A., Miller, J. M., & Cackett, E. 2019, ApJ, 884, 26

Zu, Y., Kochanek, C. S., & Peterson, B. M. 2011, ApJ, 735, 80